MEASUREMENT OF NEAR-FIELD RADIATIVE HEAT TRANSFER BETWEEN PLANE PARALLEL PLATES AT NANO-SCALE GAPS

by

Kurt David Webb

B.S, Mechanical Engineering, Kettering University, 2008

B.S, Applied Physics, Kettering University, 2008

Submitted to the Institute for Graduate Studies in
Science and Engineering in partial fulfillment of
the requirements for the degree of
Master of Science

Graduate Program in Mechanical Engineering
Boğaziçi University

2012

MEASUREMENT OF NEAR-FIELD RADIATIVE HEAT TRANSFER BETWEEN PLANE PARALLEL PLATES AT NANO-SCALE GAPS

APPROVED BY:

Assist. Prof. Hakan Ertürk . . . . . .
(Thesis Supervisor)

Prof. M. Pınar Mengüç . . . . . .
(Thesis Co-Supervisor)

Assoc. Prof. Kunt Atalık . . . . . .

Assoc. Prof. Hasan Bedir . . . . . .

Assist. Prof. Hamdi Torun . . . . . .

DATE OF APPROVAL: . . . . . .

ACKNOWLEDGEMENTS

This two and a half year project culminated in experimental measurements of nano-structured, bonded and diced samples. This required the efforts of many people for whom and for whose contributions I am deeply grateful.

I want to thank Prof. M. Pınar Mengüç, my advisor and the project leader for initiating this project and having the optimism and steadfastness to keep the group inspired and forward moving as we faced challenges that seemed insurmountable. I cannot thank him enough for all of his support throughout the project and for the extraordinary opportunity to work on this project. Above all, I will never forget the fact that he has been more like a father than a teacher for me. To Hakan Ertürk, my advisor, I thank for his astute attention to detail and ability to apply the scientific method critically to all necessary experimental aspects. He showed me the importance and applicability of theory to both calculate experimental results and to quantify the accuracy of experimental measurements and results. I truly appreciate the opportunity I had to work with him.

To Tuba Okutucu, I thank for her leadership in the sample fabrication. She helped guide the project well by having the foresight to anticipate and overcome many obstacles in sample fabrication. To Zafer Artvin, the master's student in charge of sample fabrication, I thanks for the superb job working at multiple facilities to nano-structure and dice the wafers as well as coordinating with international companies to bond wafers together. To Farhad Kazemi Khosroshahi who has taken on this experiment, I would like to thank first for his curiosity and attention to detail in learning the method for conducting experiments with the setup. I appreciate his good work ethic applied to this experiment taking many measurements and doing 3D calculations to help us interpret the experimental results. I also owe much thanks to İbrahim Mutlu the Mechanical Engineer at Boğaziçi University who very precisely machined the many necessary custom parts for the setup.

In addition, I cannot forget to mention my friend and former colleague, Yiğit Uysallı who helped me so much on multiple occasions showing me around the labarinthian district of Karaköy where hand tools, power supplys, and so many essential parts the setup were purchased. To my wife Ebru, who helped me so much throughout and especially at the end

with organizing data and editing. Finally, I want to share my appreciation for my friends and family, from Turkey and the United States, for all their support. Without my parents in the US, telling me always “work hard” and my friends in Turkey, telling me “kolay gelsin” (may it [the work] come easily to you) this would not have been nearly as rich an experience, as it has been.

I would also like to acknowledge that this research project has been carried out as a part of Istanbul Collaborative at the Center for Energy Environment and Economy at Özyeğin University. Funding for the project was provided by TÜBİTAK (the Scientific and Technological Research Council of Turkey) under 1001 Program Grant No. 109M170 and by EU FP7 Marie Curie IRG Program NF-RAD Project. Prof. M. Pınar Mengüç at Özyeğin University for both grants was the project leader.

ABSTRACT

MEASUREMENT OF NEAR-FIELD HEAT TRANSFER BETWEEN PLANE PARALLEL SILICA-THIN FILMS

This thesis establishes a methodology and experimental setup for measuring radiative heat transfer between nano-spaced plane-parallel plates. It uses a setup with two plane-parallel substrates, one heated, one cooled, at a fixed distance from one another. The temperature measurements are carried out by temperature probes on each substrate. The heat flux input is provided by an external focused laser source. The measurement of flux is carried out by diverting a percentage of the incoming light to a photodiode. The stabilization of heat flux is achieved by passive cooling. The measured data are to be evaluated based on its comparison with published numerically calculated results, which indicate an exponential increase in net radiation heat transfer as plate spacing decreases from 100 to 1nm.

ÖZET

Bu tez, arasında nano boyutta mesafe bulunan paralel plakalar arasındaki ışımalı ısı transferi için deney kurulumu ve yöntembilimi sunmaktadır. Bu kurulumda bir tanesi soğutulan, bir tanesi ısıtılan ve aralarındaki uzaklık sabit olan iki paralel plaka kullanılmıştır. Sıcaklık ölçümleri her plakanın üzerindeki alıcılar tarafından yapılmıştır. Sisteme giren ısı akışı, dışarıdan odaklanmış lazer kaynağı tarafından sağlanmış ve sisteme giren bu ısı akışının ölçümü, gelen ışının belli bir yüzdesinin fotodiyota yönlendirilmesiyle yapılmıştır. Isı akışının dengelenmesi ise pasif soğutma ile sağlanmıştır. Ölçülen veriler, literatürdeki hesaplanmış veriler ışığında değerlendirilmiş, bu değerlendirme sonucunda plakalar arası mesafe 100 nm'den 1 nm'ye inerken, ısı transferinde üstel bir artış gözlemlenmiştir.

TABLE OF CONTENTS

LIST OF FIGURES

LIST OF TABLES

LIST OF SYMBOLS

A	Cross-sectional area of plate through which heat is transferred
A_c	Area of the hot plate from which heat is conductively and radiatively transferred to the environment
A_{gap}	Measured area of the wafer surface minus the wall area
A_h	Area of the hot plate from which heat is conductively and radiatively transferred to the environment
A_{min}	Minimum area of the silica pillars or walls necessary to hold the adjacent silicon wafer
A_{rad}	Area of the plates from and to which heat is radiatively transferred
A_{rod}	Cross sectional area of copper protrusion
A_w	Cross sectional area of the silicon dioxide walls between plates
d	distance between plates' surfaces
D	theoretical orifice diamer for approximation using Nyquist noise formula
D	flexural rigidity
D^2	gives the squared electric-field amplitude of the evanescent surface modes
d_c	lattice constant
E	Total energy emitted by a body
E_{100}	Modulus of elasticity for a (100) oriented crystalline silicon plate
e_∞	is the high frequency dielectric constant
g	Gravity
h	Planck's constant
$h(d,T)$	Heat transfer coefficient as a function of length and temperature
h_c	Heat transfer coefficient for receiver
h_{eq}	Equivalent heat transfer coefficient for surface representing a heat spreader or cooler
h_h	Convective heat transfer coefficient for emitter
$h_{h,d}$	Convective heat transfer coefficient of horizontal down-facing surface
$h_{h,u}$	Convective heat transfer coefficient of horizontal up-facing surface

$h_r(d)$	Near-field radiative heat transfer coefficient
h_v	Convective heat transfer coefficient of vertical surface
I_l	current
J_{th}'	Area independent thermal contact resistance at a specified interface
J_{th}	Total area independent thermal contact resistance
k_{air}	Thermal conductivity of air
k_B	Boltzmann constant
k_{C11000}	Thermal conductivity of Copper 11000
K_{in}	Thermal conductance of TEC
k_{Si}	Thermal conductivity of Si
k_{SiO2}	Thermal conductivity of polycrystalline glass
l	plate length
M	Moment
p	Intensity of a distributed load
P	Distributed load
P_e	Electric power needed to drive the peltier-cooler
$q_{h\text{-}c}$	Heat flux between emitter and receiver
Q_c	The heat into the cooler from the sample
$Q_{c,conv}$	Heat convectively transferred to environment from receiver
$Q_{c,rad}$	Heat radiated from the receiver to environment
$Q_{h,conv}$	Heat transferred convectively to environment from the emitter
$Q_{h,rad}$	Heat radiated from the hot plate to environment
$Q_{h\text{-}c}$	Heat transferred from emitter to receiver
$Q_{h\text{-}c,air}$	Heat conducted through air from the emitter to the receiver
$Q_{h\text{-}c,rad}$	Heat radiatively transferred from the emitter to the receiver
$Q_{h\text{-}c,wall}$	Heat transferred through walls from the emitter to the receiver
Q_i	laser heat incident on the sample
Q_{meas}	Amount of heat diverted by beam splitter to power meter during experiments
$Q_{out,cond}$	Heat out of the sample by conduction to copper protrusion
R	Coefficient for the beam splitter representing Q_i divided by Q_{meas}
R_{in}	Internal electrical resistance of thermal electric cooler legs
T	Temperature
T_∞	Temperature of the surroundings

T_c	Measured temperature of receiver
$T_{c,Rod}$	Temperature measured on the copper rod closest to sample
$T_{c,surf}$	Calculated surface temperature of receiver
T_{cj}	Temperature of TPV cell's junctions between the plate that cools the sample and the thermoelectric pillar
T_h	Measured temperature of the emitter
$T_{h,Rod}$	Temperature measured on the copper rod farthest from sample
$T_{h,surf}$	Calculated surface temperature of emitter
T_{hj}	Temperature of TPV cell's junctions between the plate that dumps heat and the thermoelectric pillar
t_{Si}	thickness of Si wafer
t_{SiO2}	thickness of SiO_2 thin-film
T_{wall}	Temperature of the surrounding walls
$\forall_{Si}$	Volume of the silicon wafer
w	width of sample
w_w	wall width
x_1	distance along protrusion between copper spreader and thermocouple 1
x_2	distance along protrusion between copper spreader and thermocouple 2
α	Absorptivity
α_{pn}	Seebeck Coefficient (Overall)
α_{ra}	numerical factor dependent on ratio of length/width
Γ	damping coefficient
ΔT	Difference between T_h and T_c
ΔT_{Rod}	difference between temperatures $T_{h,Rod}$ and $T_{c,Rod}$ measured along copper protrusion (rod)
ΔT_{surf}	Difference between $T_{h,surf}$ and $T_{c,surf}$
Δx	distance along protrusion between thermocouples x_2-x_1 used to measure ΔT_{Rod}
ϵ_{Si}	emissivity of Si
ε''	imaginary part of the dielectric function
ε'	real part of the dielectric function

ε_h	emissivity of emitter
ε_c	emissivity of receiver
$\Theta(\nu,T)$	Frequency and temperature dependent oscillatory function
ν_{LO}	longitudinal optical phonon frequency
ν_p	poisson's ratio
ν_{TO}	transverse optical phonon frequency
ξ	d multiplied by surface tangent wave vector component
ξ_c	maximum ξ over which the weighing function is integrated
ρ_{Si}	density of silicon
τ_{ave}	average shear
$\tau_{max,SiO2}$	max shear strength silica
$X(\nu)$	frequency dependent weighing function
ω	Uncertainty
ω_A	Uncertainty in area through which heat is transferred
ω_{ARod}	Uncertainty of rod area
$\omega_{Jth'}$	Uncertainty in individual area independent contact thermal resistance
ω_{Jth}	Uncertainty in total area independent contact thermal resistance between plates
ω_{kair}	Uncertainty in conductivity of air
ω_l	Uncertainty in length of sample
$\omega_{Qc,rad}$	Uncertainty in heat radiated from cold plate to surroundings
$\omega_{Qh,rad}$	Uncertainty in heat radiated from hot plate to surroundings
$\omega_{Qh\text{-}c}$	Uncertainty in heat transferred from hot to cold plate
$\omega_{Qh\text{-}c,air}$	Uncertainty in heat transferred by conduction through air from emitter to receiver plat
$\omega_{Qh\text{-}c,rad}$	Uncertainty in heat transferred radiatively from hot to cold plate
$\omega_{Qh\text{-}c,wall}$	Uncertainty in heat transferred by conduction through walls from hot to cold plate
ω_{Qi}	Uncertainty of Q_i
ω_{Qmeas}	Uncertainty of Q_{meas}
$\omega_{Qout,cond}$	Uncertainty in measured heat conducted out of the sample through copper rod
ω_{Qrad}	Uncertainty in heat radiated from sample to surroundings
ω_R	Uncertainty interval of R
$\omega_{Tc,surf}$	Uncertainty in calculated surface temperature of cold plate

$\omega T_{h,surf}$	Uncertainty in calculated surface temperature of hot plate
ω_w	uncertainty in width of sample

LIST OF ACRONYMS/ABBREVIATIONS

1D	One Dimension
AC	Alternating Current
AFM	Atomic Force Microscope
CO_2	Carbon Dioxide
COP	Coefficient of Performance
DA	Derganjuin Approximations
DAQ	Data Acquisition Unit
DC	Direct Current
EM	Electromagnetic
He	Helium
InSn	Indium Tin
n-doped	negatively doped
p-doped	positively doped
PV	Photo Voltaic
RMS	Root Mean Squared
SiC	Silicon Carbide
SiO_2	Silicon Dioxide, Silica, Glass
SPhP	Surface Phonon Polaritons
TEC	Thermo Electric Cooler

1. INTRODUCTION

The 2012 world is as interconnected as it has ever been. People are living lives that depend on goods and services from across the world. Almost all of the transport and the goods produced and transported depend now on hydrocarbons for energy production. Even basic needs such as food and water are met using energy from hydrocarbons. Hydrocarbons such as oil, coal, and methane or natural gas remain from life that lived on earth many millions of years ago. It has taken 500 million years for the supply of oil and coal within the earth's crust. It is being removed much more rapidly than it is being replenished. Unless there are new and renewable energy sources available, a time should come when there will be no accessible fossil fuels on earth or when those existing fossil fuels will be too difficult or expensive to extract. Currently oil companies seek extravagant means for oil production including deep sea drilling which puts drill workers at high risk of losing their lives and puts the oceans' wildlife and habitats at risk in the case of an oil leak or disaster. Coal mining similarly puts miners' lives at risk. New methods of obtaining natural gas such as hydraulic fracturing of shale, known as fracking, expands the amount of available natural gas, but have caused fractures up to 588 m (Davies *et al*., 2012). Wastewater deposition from fracking into wells are thought to have caused 3.3 and 4.0 magnitude earthquakes by lubricating existing fault lines (Zoback *et al*., 2010) (Martineau, 2012). Since wells are below aquifers, drinking water contaminations due to leaks through seals have also occurred.

Another drawback to using fossil is when burned or used they emit carbon dioxide (CO_2) which is a well-known greenhouse gas. The predicted effects of the increase in world temperatures have brought the world's nations' leaders together in climate summits such as the in UN Summit in Copenhagen in 2009, in Cancun in 2010 and in Durban in 2011, as well as in the People's Climate Summit in Bolivia. Amidst these warnings about the use of fossil fuels, there is a steady increase in world demand for energy. The ways to take on the challenge of reducing CO_2 emissions presented include: increasing usage of renewable sources of energy such as sun, wind as well as carbon dioxide free energy from non-renewables via nuclear fission, and by sequestering or finding uses for the CO_2

byproduct of coal power plants. It also means using energy more economically. One of the ways to increase the efficiency of energy usage is the recovery of waste heat from high temperature systems. One example of this is the recovery of electrical energy from the excess heat from the cooling of glass after leaving glass furnaces. One device that may be used for recovering waste heat as electricity is a thermophotovoltaic (TPV) cell.

TPVs are photovoltaic (PV) devices operating similar to solar-photovoltaics (SPVs) that convert incident radiant heat from the sun to electrical power by inducing a current. The main difference between SPVs and TPVs is the wavelength range of the conversion. The heat incident on a TPV is of a much wider spectrum, therefore filters and emitters are used to reduce the spectral width of the incoming photons. This is because only a narrow wavelength band is desired for efficient energy conversion in either system.

The PV is the part of the TPV or SPV responsible for converting incident radiant heat energy into an electron current via the photovoltaic effect. The individual components of a standard PV cell must be described, explaining how incident photons generate an electric potential in order to understand the PV effect.

A PV cell is comprised of two oppositely doped semiconductors as shown in Figure 1.1. The first layer, where the electromagnetic (EM) energy (referred to as photons in most cases) is incident is positively doped (p-doped) with doping atoms that create free positively charged carriers known as holes. The second layer is negatively doped (n-doped) with atoms that create free electrons as charge carriers. If silicon is used as the semiconductor, boron and phosphorous can be used for p-doping and n-doping respectively as shown in Figure 1.1. The interface between the two layers is called the junction. Holes from the p-layer and electrons from the n-layer diffuse across the junction until equilibrium is reached.

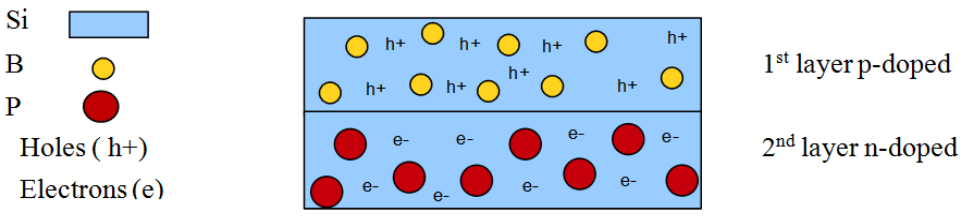

Figure 1.1. P and n-doped silicon wafer.

At equilibrium there exists a region, spanning from part of the p-doped over the junction to the n-doped layer, as shown in Figure 1.2, that is depleted of carriers. This region is called the depletion region. The top part of the depletion region has stable positively charged boron ions and the bottom part is scattered with stable negatively charged phosphorous ions. Due to this charge gradient across the junction, a positive electric field from the p-doped towards the n-doped region is formed. Above and below the depleted region are neutral p-doped and n-doped regions, respectively as shown in Figure 1.2 (Kasap, 2000).

In a direct band-gap semi-conductor, electrons jump from the valence band to the conduction band when given the necessary energy deficit between levels. That energy deficit between the valence and conduction band is called the band-gap. When incident photons with a higher energy than or equal to the band-gap energy are absorbed in the depletion region, electron hole pairs are created in a direct band-gap semiconductor PV cell. A hole is the positive analog of an electron. These electrons are split from the holes by the intrinsic electric field that exists within the depletion region. As many electron hole pairs split, charge builds at the p and n doped regions. This buildup of charge is a useable electric potential. Counteracting this creation of electric potential are the photons absorbed in the neutral p and n doped layers of the PV. This is because they create hole electron pairs that diffuse towards the depletion region to neutralize the electrons or holes coming from the depletion region. Because of this neutralizing effect, the photovoltaic must be designed so that most of the photons are absorbed in the depletion region (Basu *et al*., 2006).

The difference between TPV and SPV is mainly the energy source. For SPVs the source is the sun while for TPVs the source may be a variety of heat emitting sources. The heat received by a TPV is also different because it is of a much higher concentration than that received by SPVs because TPVs are used in a closer proximity to their radiation source.

The source radiation also differs in terms of wavelength and wavelength range of their emitted radiation. The wavelength spectrum of energy emitted by a hot body is based on Planck's black-body radiation. The radiation emitted for black bodies at 5780 K and

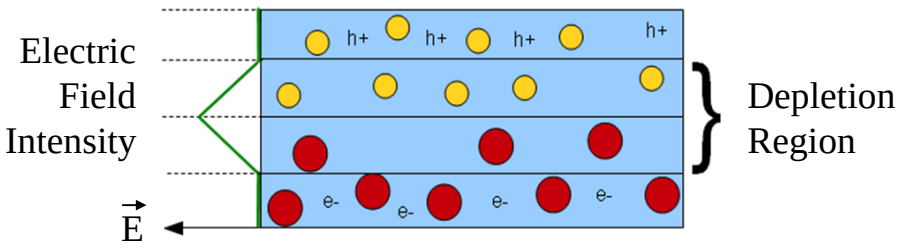

Figure 1.2. Electric field and depletion region.

1600 K are shown by wavelength in Figure 1.3.

The Sun can be approximated as a blackbody heat source at 5780 K, whereas blackbody at 1600 K represents a possible source for TPVs. From Figure 1.3, the peak wavelength emitted by the Sun is 0.485 μm (visible green) and the full spectral width is 0.580 μm at half the maximum energy. For a source at 1600 K, the peak wavelength of emission is 1.8 μm, (near infrared) with a full spectral width of 2.2 μm at half the maximum energy. The peak energy emitted by a black body at 1600 K is also three magnitudes lower that a blackbody at 5780 K. Although radiation incident on TPVs have a

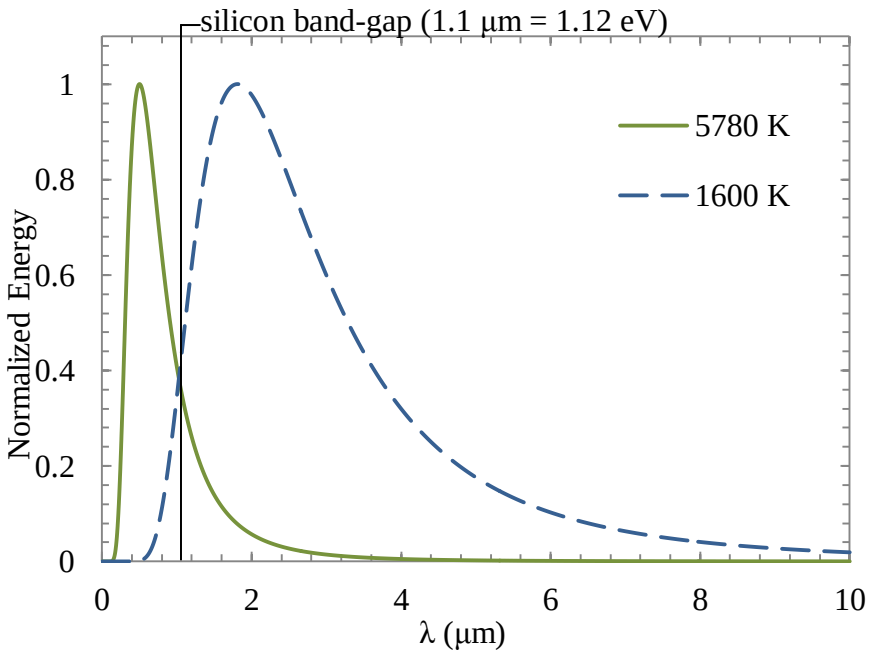

Figure 1.3. Plank's blackbody radiation for Sun (left) and source at 1600K (right).

wider spectrum, much of the incident radiation including part of that above and all of that below the band gap cannot be used for generating a current as the PV effect takes place only at discrete band gaps.

The wavelengths emitted in comparison with the PV cell's band gap are also shown in Figure 1.3. The EM energy absorbed at and below the PV's wavelength band-gap can generate a voltage in the TPV. The EM waves with longer wavelengths cannot generate a voltage and instead transfer radiant heat to the PV or are transmitted. The EM energy of shorter wavelengths (higher energy) transfer part of their energy as an added voltage; the remainder heats the PV cell. The heating of the cell reduces efficiency. (Skoplaki and Palyvos, 2008) Because a much greater portion of the total radiation in TPV sources can generate heat as opposed to SPVs, additional parts are used for TPVs to filter the radiation that is received by the PV. A TPV may be comprised of either three or four main parts. Two are: heat source, and photovoltaic cell just as in SPV. The other parts include a filter and or an emitter. Figure 1.4 is shown with both an emitter and a filter. Using these filters, the PV cell only receives photons that match or nearly match the band gap of the PV cell.

The emitter shown in Figure 1.4 absorbs incident radiant heat from the source, and emits radiation at a much narrower spectral band. The emitter must have spectrally selective radiative properties. In order to maximize the TPV performance; the emitter must have a high emissivity in the band-gap, or band-gaps of the PV cell as shown in Figure 1.4, and must have a high absorptivity at the emission wavelengths of the heat source. Absorptivity for a surface depends on the direction, spectral distribution and the state of

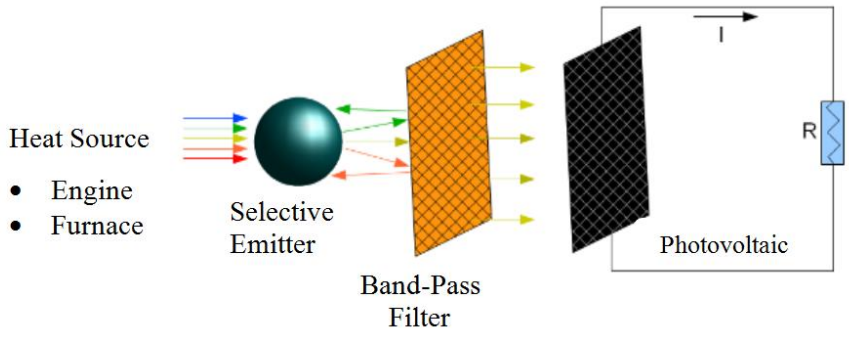

Figure 1.4. Components of TPV system.

polarization of the incident radiation (Howell *et al.*, 2010).

One group of materials that have been found to emit very narrow wavelength bands are the ions of rare earth elements when they are immersed within a crystal structure. In this configuration, electrons are extremely localized or confined. Due to this confinement of electrons, they when excited at high energies do not decay by transmitting a phonon into a lattice as it would in a bulk material. Instead the energy is emitted in narrow wavelength bands. This forms a type of photonic crystal. Photonic crystals may also be utilized on a surface. These crystals can be formed by etching surface pattern on a material which supports surface waves. Due to interference effects of surface waves on 1D photonic crystals, emission is stronger in specific wavelengths dependent upon their surface etch widths of the emitters and adjacent non emitters as shown in Figure 1.5 (Narayanaswamy, 2004).

Another way of taking advantage of quantum confinement to increase efficiency of PVs and TPVs is by using quantum dots, an effective zero-dimensional photonic crystal, to convert absorbed photons at energies much higher than the quantum dot material's bandgap to multiple lower energy electrons in a reverse Auger process (Nozik, 2002). This method has been used to fabricate SPVs, but has not yet been used to fabricate TPVs although TPVs converting light from a much wider band could have much more to benefit from this technology.

Other ways of reducing the bandwidth of the radiation traveling towards the PV are shown in Figure 1.6. The most effective filter is a band pass filter. Its advantage over low or high pass filters is it recycles the light back to the emitter that has both too high or too low of energy. The disadvantage over the high and low pass filters is the greater loss of light intensity reaching the PV because theoretically all incident light at and above the energy band-gap generates a voltage (Basu *et al*., 2006).

A typical filter functions as shown in Figure 1.6. Together the emitter and filter work to reduce the spectral bandwidth of the radiation from the heat source to a narrow band just above the energy band gap of the photovoltaic materials. This reduced

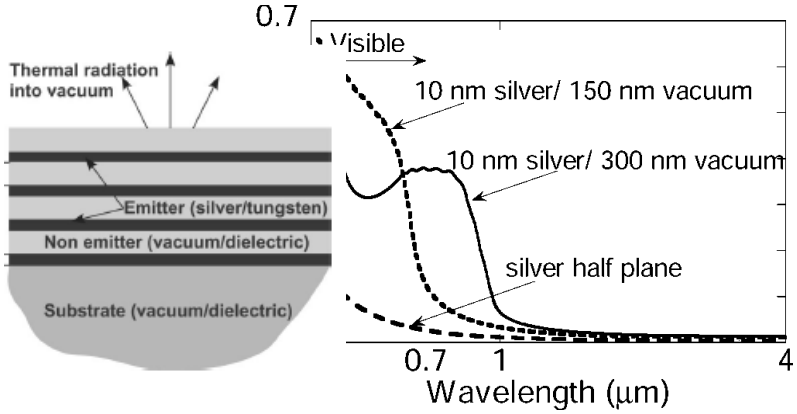

Figure 1.5. Calculation geometry and emissivity vs. wavelength (Narayanaswamy *et al*., 2004).

bandwidth light is made incident on the PV. Because of the reduced bandwidth less heat will be generated and the cell can achieve a higher efficiency.

A theoretically demonstrated way of narrowing the band of energy transmitted from the emitter to the receiver is by positioning the emitter and receiver close together to take advantage of what is called the near field effect. When two of the same material dielectric surfaces are brought into close proximity, or the near-field where the distance is less than the dominant radiatively emitted wavelength, surface waves interact and transfer from surface to surface. In this way the two surfaces interact with the other surfaces and energy can be transferred at high rates from one plate to another. This surface to surface wave interaction can occur not only across gaps, but also across the thickness of a thin-film. The effect of the near-field and thin-film effects have been calculated by Francoeur *et al*. (2008). The near field effect and the thin-film effect at narrow resonant wavelength bands are transferred between emitter and receiver as shown in Figure 1.7. Again, this occurs due to the thermal excitation of surface phonon polaritons (lattice waves observed in dielectric) which tunnel (travel across vacuum gap) from emitter to receiver. This illustrates the two main advantages for utilizing near field radiative heat transfer in TPVs, there is a higher rate of energy transfer and there's no need for a filter so there is more usable energy being transferred across the gap.

Efficiency is defined as the amount of electric power output of the TPV cell over the power incident on the cell from the emitter (Basu *et al.*, 2006). The amount of thermal

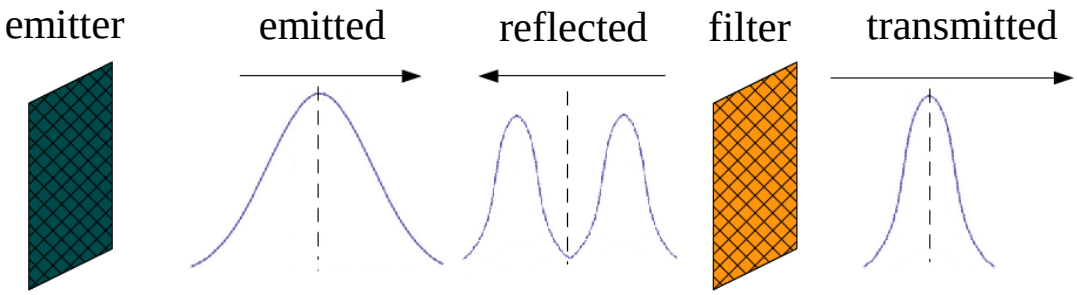

Figure 1.6. Filtering of emitted spectrum.

radiation emitted by a black-body is limited by its absolute temperature T at a wavelength λ_0 (in a vacuum) according to the Planck's spectral distribution of emissive power in Equation 1.1.

$$e_{\lambda b}(\lambda_0, T) = \frac{2\pi h c_0^2}{\lambda_0^5 \left(\exp\left(\frac{h c_0}{\lambda_0 T k} \right) - 1 \right)} \tag{1.1}$$

Here, h is the Planck constant, c_0 is the speed of light in a vacuum, and k is the Boltzmann constant (Howell *et al.*, 2010). This limit is valid for the far field, where the distance from the emitter must be much greater than the dominant, or peak wavelength of the emitted radiation. If the distance is not greater than the dominant wavelength the near-field effects must be considered, where this limit is no longer valid. In the near-field, interactions of evanescent waves can increase the amount of radiative heat transfer.

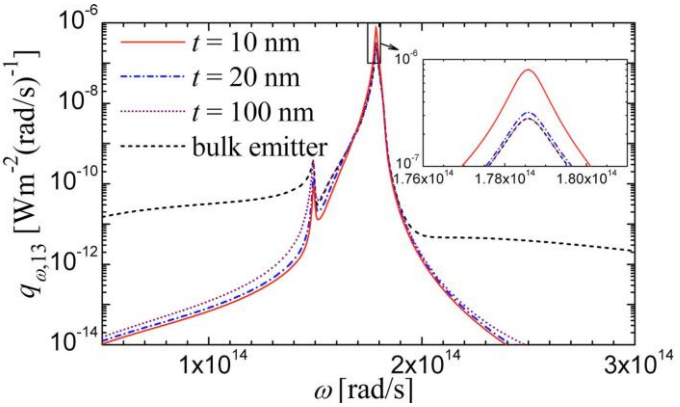

Figure 1.7. Radiative heat transfer between parallel SiC plates spaced 10 nm (Francoeur *et al.*, 2008).

(Rousseau *et al*., 2009) At gaps less than 100 nm there are coulombic interactions and for polar materials which support surface phonon polaritons (SPhP) there can be energy tunneling and interaction between these surface waves due to the existence of evanescent standing waves in these regions (Basu *et al*., 2006). Therefore, there is a possibility for a much enhanced transfer of energy between plates with nano-spacing. If applied to TPV cells the energy density of TPVs can be much enhanced without any increase in emitter temperature as would be needed in the far field regime. Although not reaching gap spacing of nano-meters, DiMatteo *et al*. (2001) have proven that by coupling emitter and receiver surfaces, the output can be increased by a factor of five. On the other hand, Francoeur *et al*. (2010) suggested that overheating of the TPV cells will decrease the performance of such systems significantly. Still, the amount and optimum spectrum of radiative heat transfer at nanoscales in relation to gap size, materials and temperature have yet to be fully experimentally proven. This thesis is to establish a measurement facility for eventual testing and evaluation of TPV systems in laboratory settings.

2. LITERATURE REVIEW

Since 1969, multiple experiments have been carried out aiming at understanding radiative heat transfer where spacing between objects is below the dominant wavelength of the emitted radiation. These experiments are also intended to explore and understand when Planck's law of blackbody radiation does not apply. Most of these experiments were performed to develop the relationship between distance between objects and total radiative heat transfer. In this Chapter, each of these experiments, the measurement method and results are analyzed. This literature review covers near field radiative heat transfer measurement in plane to plane, tip to plane and sphere to plane geometries.

The first recorded measurement of near field radiative heat transfer was made by Hargreaves in 1969, at Phillips Co. in the Netherlands. His setup consisted of two 5 cm² area parallel glass plates with surfaces, from which radiative transfer between plates occurs, plated with 100 nm of chromium. The measurements took place in a vacuum environment of 10^{-5} torr to mitigate the effects of convection between plates. Piezo-electric ceramic pillars placed between the two plates were used for adjusting the spacing and capacitance measurements were used to monitor separation distance. By separating the plates' coatings into three parts three independent capacitance measurements were possible. In order to maintain parallelism, the plates were adjusted so that all capacitances matched. All experiments were performed with hot temperature, T_h , of 323 K and a cold temperature, T_c of 306 K (See Figure 2.1). The minimum distance achieved between plates was 1.5 μm. Applying Wien's Displacement Law, (Equation 2.1) the dominant wavelength of radiation emitted from the hot plate is found to be 8.97 μm, so the measurement in this experiment was taken in the near field.

$$\lambda_{\max} = \frac{C}{T} \tag{2.1}$$

where C is 2897.7686 μm-K. We may presume that this distance was the shortest the piezo-electric pillars could hold while also maintaining a constant height. The flux was measurable because T_c was held constant and the surroundings were insulated at T_h. The

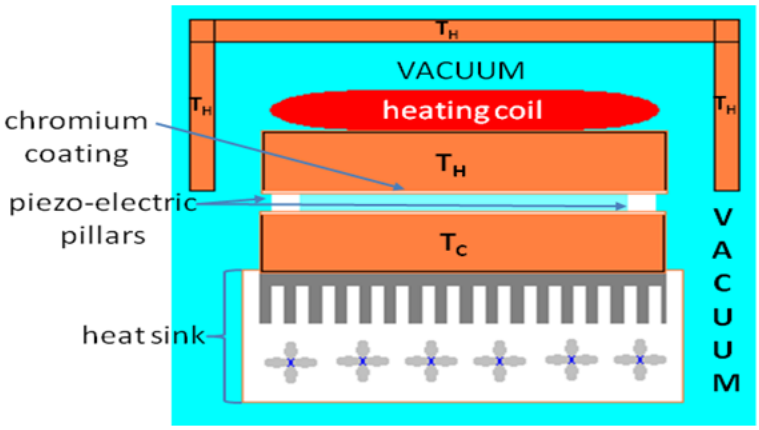

Figure 2.1. Experimental setup variable spaced parallel plates.

flux was measured and compared by adjusting the system height, then changing the flux input to achieve the T_h and T_c. The power output of the heating element was monitored. This power output was equal within 1% to the flux through the sample (Hargreaves, 1969).

Experimental techniques learned from this experiment include the plate separation, for electrically conducting plates, may be found and parallelism may be maintained using multiple capacitance measurements. This experiment also shows that high precision adjustable pillars with low heat conduction/loss may be made using piezo-electrics for gaps down to 1.5 μm.

Experimental data, as shown in Figure 2.2 demonstrated $Q_{h\text{-}c}$ vs. proximity effect down with a flux measurement error of 1% to a distance of 1.5 μm with plates of 5 cm^2 area. Here $Q_{h\text{-}c}$ represents total heat flux and d represents the uniform distance between plates. At the smallest gap, a near doubling in the flux viewed at far field was observed. (Hargreaves, 1969)

The second experiment, done measuring near field radiation heat transfer was conducted by Domoto *et al.* (1970). Their experiment, although done at cryogenic temperatures was very similar to the experiment performed by Hargreaves. The aim of the experiment was to understand the behavior of far-infrared emitted from objects at temperatures near that of liquid Helium (He). The experiment was performed and written without reference to Hargreaves' work. Just as in Hargreaves' experiment, the walls

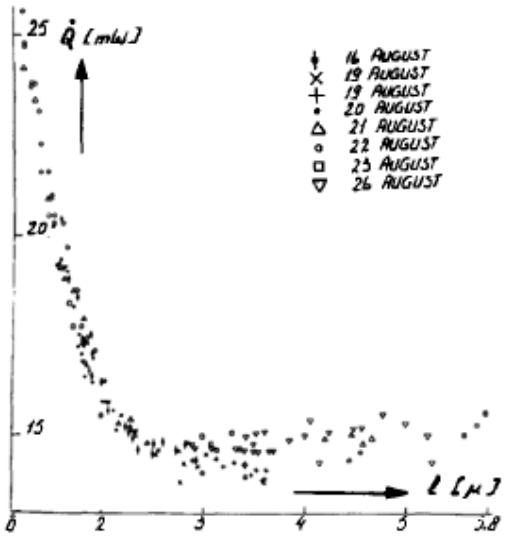

Figure 2.2. Experimental results (Hargreaves, 1969).

around the parallel plates were kept at the temperature of one of the plates. In this case however, the surrounding walls were kept at T_c not T_h (insulated around the heat source) as in the experiment by Hargreaves, the walls surrounding the hot and cold plates were kept at T_c. The walls were made of a near blackbody material, which increased the absorption of energy from the colder copper plate, aiding it in maintaining same temperature as the walls and the liquid He. Two 8.5 cm diameter solid copper plates were used for the emitter and receiver. Just as in Hargreaves' experiment, piezo-electric devices were used as the adjustable supports. The measurement of flux was done by monitoring the power into the heated base ring during steady state heat transfer. What was different about the pillars is that they were connected to the receiver and heater as opposed to the receiver and emitter in Hargreaves' experiment. The experiment took place in a vacuum environment at 10^{-12} Torr. The receiver temperature T_c was held at 4.5 K while the emitter temperatures were 10 K, 13.8 K or 15.1 K as shown in Figure 2.3. The minimum distance between plates achieved for this experiment was 10μm. The dominant wavelength of radiative heat transfer at these temperatures by Wien's Displacement Law, Equation 2.1, ranges from 192 to 290μm for temperatures 15.1 K and 10 K, respectively, indicating that these experiments took place well within the near-field. When comparing with an experiment done by Cravalho *et al*. mentioned in this paper, at 11.0 K and 4.6 K, there is an inconsistency in measurements. It is inferred by the authors that the reason for the difference is the inconsistency of the surface properties of hand polished copper (Domoto *et al*., 1970).

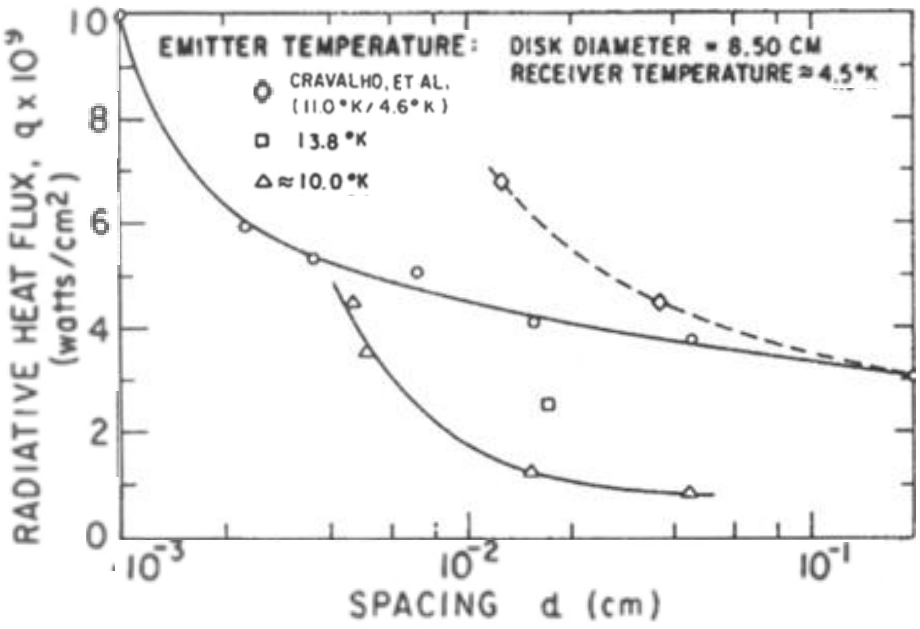

Figure 2.3. Experimental results (Domoto *et al*., 1970).

This experiment confirmed the reliability of using piezo-electrics as height adjusters and showed that the surroundings insulated at one of the two plate's temperatures, either T_H or T_C, is a viable way of achieving steady state temperatures while being able to measure flux. It also confirmed that it is possible to measure the flux through the sample by monitoring the flux into the hot plate.

In 1994, heat transfer between two metallic surfaces at small distances was measured by Xu *et al*. (1994). This experiment was done by quite a different method than those used by the previous two studies. Xu *et al*. (1994) used a thermocouple formed by vapor deposition of Ag90 and $Cu_{10}Cr$ to form a 160x160 μm^2 junction on the surface of a glass plate to measure temperature. An indium needle was flattened against the glass plate in order to create a 200 μm diameter circular plane at its end, and the flattened end surface of the needle was placed in parallel with the deposited thermocouple. The glass plate's parallelism with the needle was measured using an optical interference microscope. It was determined using diffraction microscopy that the tilt angle kept between surfaces was less than 0.15°. The indium needle was heated via a heat coil. The gap between needle and thermocouple was adjusted using a piezo-electric tube from the head of a scanning tunneling microscope which was held on to the housing of a micro-positioner and attached

to the needle. During measurements, the gap between the plane parallel tungsten plate and thermocouple was measured using a capacitive detector. An aluminum sheet covering the needle prevented the electrically driven piezo-electric tube from interfering with the capacitance measurements as shown in Figure 2.4. The system spacing between needle and thermocouple was zeroed at first contact between plates. Bending of the plate was avoided by attaching one side of the glass to a spring in case pressure was exerted on the glass plate, due to Coulombic or electro-static forces, or temperature changes. The authors devised their own method to for measuring proximity effects or near field effects of radiative transfer. The first proximity effect is the dying out of propagating longer wavelengths transferred between two plates due to the restriction of the electronic mean free path. The other proximity effect at very small distances is the one causing near-field enhancement, the tunneling of energy due to the interaction of surface waves.

They proposed another method for estimating flux at short distances between metals. The reason for this approach was because the other calculations needed direct numerical simulations or were too complicated to draw the simple conclusions needed for the experiments. Their preferred approach was based on the charge fluctuations described by the fundamental Nyquist noise formula. The distances they used were all below 1 μm, which put their limit much below 9.7 μm, the dominant wavelength based on Wien's Displacement Law for a temperature of 300 K. Therefore, their method safely assumes all propagating modes have phased out. The method accounts for only non-propagating modes as being responsible for all heat transfer. The characterization of a non-propagating

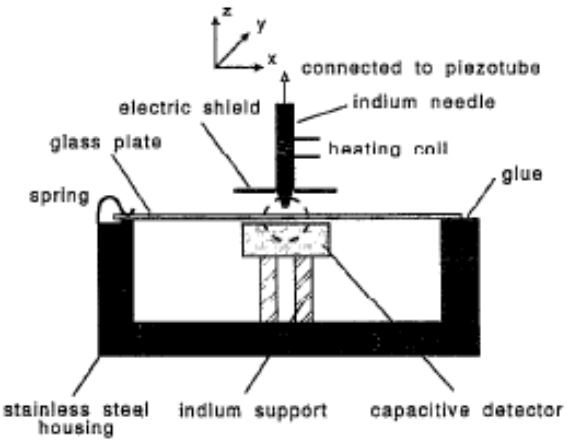

Figure 2.4. Experimental setup (Xu *et al*., 1994).

mode or near-field mode of heat transfer is connected with an alternating current (AC) flowing between the two regions parallel to their surfaces or a coupling of surface waves. This flow of AC is connected with alternating positive and negative surface charges and can be characterized by measuring the electrical resistance between the two plates at different AC frequencies. The resistance is too difficult to calculate, but is found to be on the order of magnitude of contact resistance. Geometrically it is reasoned that although the calculation cannot be made between two hemispheres of diameter D, distance D/2 apart, this is on the same order of magnitude of a D diameter orifice at the surface of a metal and it's contact resistance with a point on the metal surface in the direction of the radius of the orifice until infinity. Using D and the specific electrical resistance of the metal, the contact resistance is calculated. Using the contact resistance, the voltage noise given by the Nyquist formula was calculated. The voltage noise over the distance $D^2/4$ gives the squared electric-field amplitude of the evanescent surface modes. If the half sphere orifice is one radius length away multiplying by the dielectric constant for a vacuum the energy density in the vacuum gap is found. Using this one may find the thermal flux and that it has a $8/D^3$ dependency at these distances until the distance reaches the electronic mean free path. Figure 2.5 shows their estimate along with Hargreaves' result Stefan-Boltzmann Law, conduction by air, and Polder-Van Hove's prediction which was the current theory. Thermal drift of the piezo-electric tube was 1nm/min. Measuring DC across the sample, the contact resistance, and the alternating flux across the sample, the maximum measureable direct flux was 20mW. The conclusion of this experiment was that the theory previously proposed by Polder and Hove predicts extra coupling between surfaces. In this experiment heat transfer between indium needle flattened tip and the junction was observed only when contact was made. Therefore the sensitivity of their measurements was not high enough. Xu *et al*. (1994) conclude that findings in previous experiments, Williams and Wickramasinghe, (1986) and Martin *et al*., (1988) must have been due to conduction through a film of liquid between the thermal probe tip and sample.

Although this experiment was not successful in having the sensitivity necessary to measure the near-field effect, it suggests some new methods for measuring near field flux such as using thermocouples as the receiver. It also uses piezo electric devices for

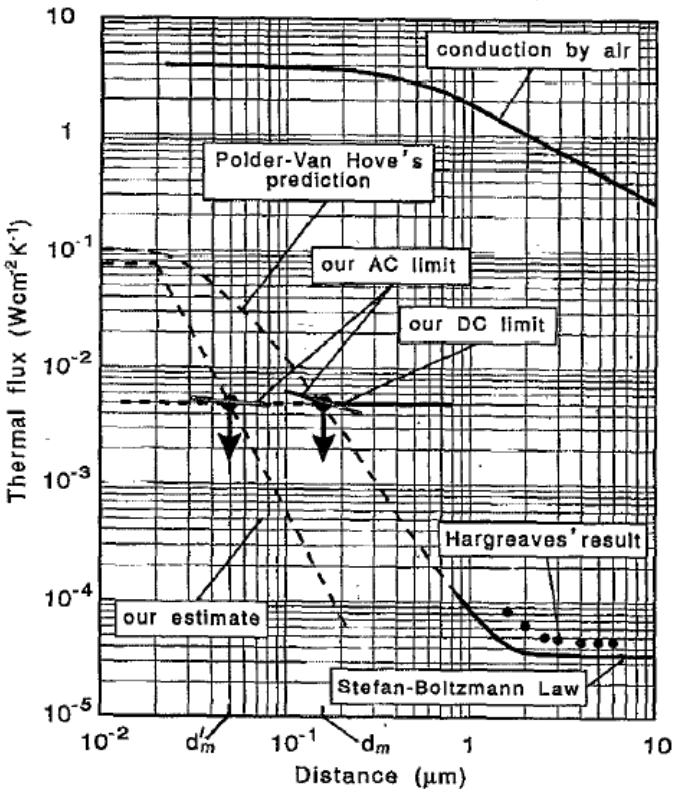

Figure 2.5. Expected results (Xu *et al.*, 1994).

positioning, which must be the most controllable device for an experiment requiring this much precision. It adds to the tools in measuring the distance, showing the usefulness of interference microscopy for measuring parallelism between plates. Although not mentioned in this paper, the surface plasmon polariton resonances of the plates are dissimilar since they are of different materials. Because of this, no resonance between these plates is observable. This illustrates the importance of using plates of the same material.

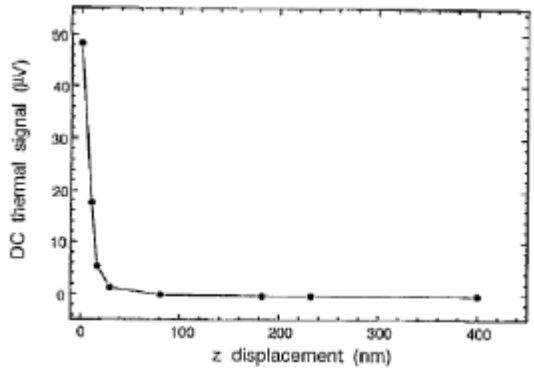

Figure 2.6 Experimental Results. (Xu *et al.*, 1994)

In a more recent experiment by Kittel *et al*. (2005) a variable-temperature scanning tunneling microscope (STM) is used as shown in Figure 2.7. This allowed for a very fine adjustment of tip to plane spacing, on the order of 1 nm. Since the tip was made with one type of metal strung through to the bottom and in contact with the metal used to plate it, a temperature dependent Seebeck voltage is created at the junction between the gold film plating and the inner platinum wire tip. These voltages were monitored for tip temperature information. By monitoring the wire base temperature, the tip temperature, the temperature of the sample and by knowing the conduction properties of the wire, the near-field radiative heat transfer is measurable.

With this tip to surface setup, flux measurements were possible with spacing to 2 nm. The results showed that fluctuating electrodynamics which had previously been used in predicting the amount of heat transfer between objects, does not fit below about 50 nm as may be seen in Figure 2.8, where dashed line representing the predicted flux using fluctuating electrodynamics. In order to correct the theory to represent the experimental data, a correlation length for both the tip and for the sample surface was proposed. Using their correlation length the solid curve in Figure 2.8 was obtained (Kittel *et al*., 2005).

Another experiment was carried out by Hu *et al*. (2008) showing the near field enhancement between plane parallel surfaces made of a polar material (Figure 2.9). Glass was chosen as the material due to its surface phonon polariton resonance, which is well

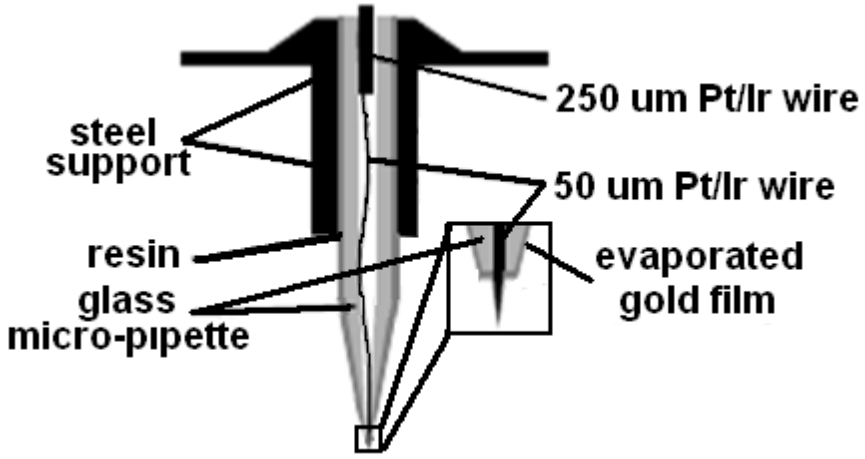

Figure 2.7. Experimental Setup (Kittel *et al*., 2005).

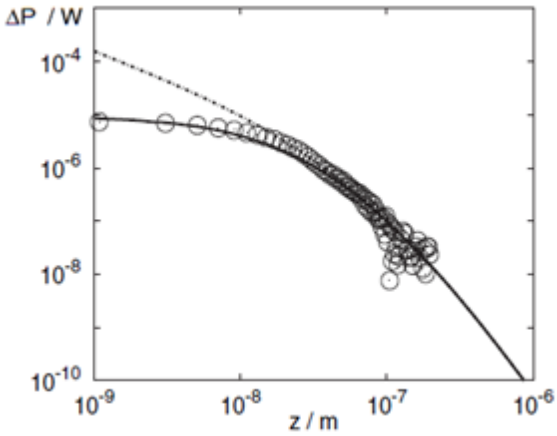

Figure 2.8. Experimental Results. (Kittel *et al*., 2005).

aligned with the peak of Planck's blackbody distribution for a body at 300 K, approximately 10 μm. The surface plasmon polaritons for metals observe resonance at much lower wavelengths, emitted as dominant wavelengths at much higher temperatures. Therefore it is much easier to observe near field enhancement of radiative heat transfer in glass and other polar surface phonon polariton supporting materials as opposed to metals.

Using the Lorentzian model to interpolate data points between 100 and 26.67 μm, a gap dependent heat transfer coefficient defined as, $h_r=q_{h\text{-}c}(T_h\text{-}T_c)$, calculated for smaller gaps. According to this calculation, at a gap of 1 μm, the coefficient of radiative heat transfer is 50% higher than that for a black body (Figure 2.10). The experiment is carried out in this range in order to show the heat transfer between parallel glass plates with a spacing of 1.6 μm as ΔT between cold and hot plates vary in order to clearly show, with

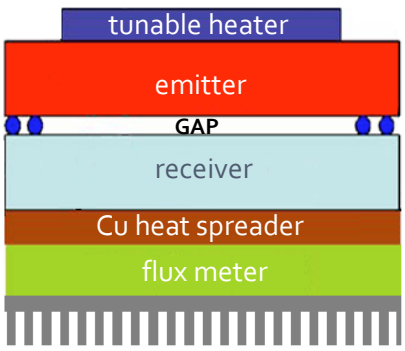

Figure 2.9. Experimental setup (Hu *et al*., 2008).

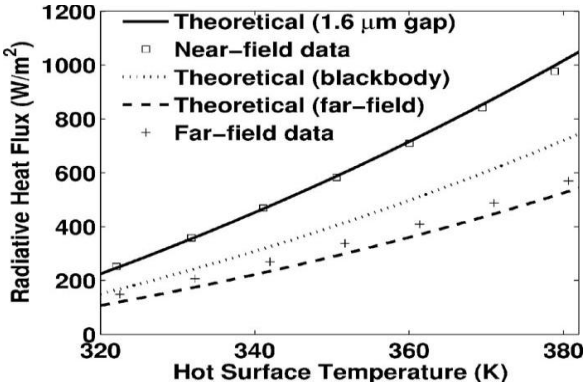

Figure 2.10. Experimental Results (Hu *et al.*, 2008).

plane parallel plates, Planck's black body limit for radiative heat transfer can be exceeded. The spacing of the plates was held using polystyrene spheres which have the property low contact area due to shape and low heat conductance due to material. The spheres, immersed in deionized water, were spread onto the surface of one of the glass plates. The water evaporated from the plate and left a residue of the micro spheres. The other plate was then placed atop the spheres. The experiment was carried out in a vacuum chamber at a pressure of 8.5×10^{-3} Pa (Hu *et al.*, 2008).

The experiment was able to show an amount of 35% heat transfer enhancement to far field radiant heat exchange for parallel black plates considering the temperatures of the two plates (Hu *et al.*, 2008).

This experiment showed the possibility of using micro or nano-spheres as spacers due to their low contact area. It also underlined the importance of using polar materials as opposed to metals for ease of observing near field effects. This experiment states that conduction through the spheres account for less than 2% of heat transfer, but this is not supported by any evidence, so it is difficult to understand how the authors came to this conclusion.

Another experiment was done by Narayanaswamy *et al*. (2008) with a sphere to plane geometry as shown in Figure 2.11. This experiment was conducted in order to show precise measurements that confirm or reject past theoretical studies and predictions about near-field enhancement of radiation heat transfer. It especially sets out to show exceeding Planck's limit for black body radiation for the sphere to plane geometry. The experiment

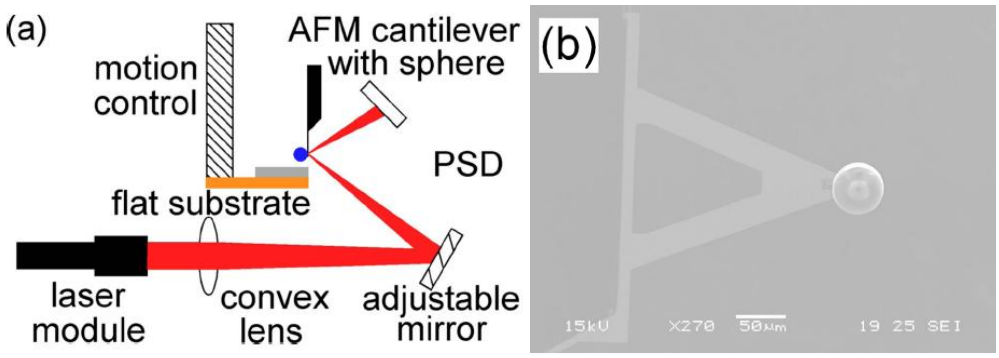

Figure 2.11. Experimental Setup (Narayanaswamy *et al*., 2008).

also aimed to provide insight about the Casamir force and its thermal contributions which had never been experimentally detected (Narayanaswamy *et al*., 2008).

In the setup shown in Figure 2.11, a bi-material atomic force microscope AFM cantilever was used for the temperature and flux measurement. Bi-material cantilevers bend in response to thermal fluctuations due to the differing coefficients of thermal expansion of the two materials. The bend in this experiment was observed by monitoring the direction of reflection from the laser heating device. Using bi-material cantilevers, temperature fluctuations as low as $5x10^{-10}$ K were measureable. With a ΔT of 50 K the measurable conductance is 10^{-11} W/K. The theory predicted for two 50 µm spheres, as an approximation for a 50 µm sphere and substrate, a conductance of 10^{-9} to 10^{-8} W/K for 100 nm to 1 µm gaps. Therefore, it was reasoned that an AFM had enough sensitivity to measure conductivity for a 50 µm sphere to plane geometry (Narayanaswamy *et al*., 2008).

The microsphere was mounted to the cantilever tip of the AFM. A silica microscope slide attached to a motion control stage was used as the planar substrate. The experiment took place in a vacuum at $6.7x10^{-3}$ Pa. as radiation becomes the dominant form of heat transfer under 0.1 Pa. The substrate temperature equaled the temperature of the environment, therefore it could be reasoned that the view factor, for far field transfer between sphere and its surroundings, is approximately one (Narayanaswamy *et al*., 2008). There was no mention in this experiment about taking into account the near field limit of propagating radiation as was discussed in the paper by Xu *et al*. (1994). Heat absorbed by cantilever, heat transfer between sphere and substrate, and the temperature of sphere must be quantified to measure the near-field heat transfer for this setup. The heat absorbed by

cantilever was estimated by measuring the emitted, reflected and transmitted laser radiant power. Through these measurements, absorptance was predicted as 0.13. Heat transfer between sphere and substrate, was predicted by monitoring the deflection of the cantilever, which was converted to heat transfer between the sphere and substrate by varying the power of the incident laser beam. Using the cantilever conductance and the heat absorbed at the tip, the temperature rise of the sphere was calculated to be 46.5K, presumably from environment temperature.

The noise or scatter in the experimental data was 0.44 nW/K and caused by the turbo-molecular pump. Positional accuracy was 100 nm. Figure 2.12 presents radiation transferred via the near-field effect only and subtracting the far-field radiation, describing the increase in near-field radiative transfer from the value of heat transfer (far-field) measured at a distance of approximately 9 μm. To understand the amount of heat transferred from sphere to plane as opposed to that transferred to the rest of the environment, the emissivity of the sphere was needed. The emissivity for the silica sphere, of diameter 50μm was calculated to be 0.97 using the Mie scattering theory. The maximum measured conductance was 6 nW/K that represents near-field enhancement, or radiation exchange above the Planck limit for a blackbody. If the far field radiative heat transfer is added, the total conductance measured was 29 nW/K (Narayanaswamy *et al*., 2008).

The experiment performed by Rousseau *et al*. in 2009 with the same geometry included a heated surface and a sphere at different distances, mounted on a cantilever,

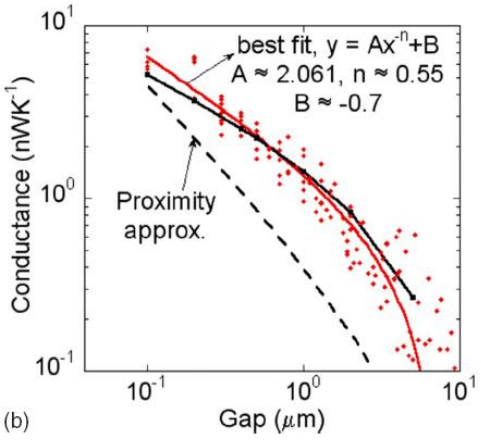

Figure 2.12. Experimental results (Narayanaswamy *et al*., 2008).

bending according to its temperature. This setup is presented in Figure 2.13. The cantilever is mounted on a piezo electric column that positions the sphere/cantilever. The cantilever's position instead of being measured by reflection angle, is measured using a pulsed laser which measured the distance of the cantilever tip from the laser. Since the bend of the cantilever also affects the sphere's distance from the heated plate, a feedback loop connecting piezo-electric positioner ensured a correct distance d as shown in Figure 2.13. A type K thermocouple was used to monitor the heated plate/emitter temperature. The experiment varying distance from sphere surface to plate, with a constant ΔT of 21 K, was carried out using a sphere of diameter 40 μm and a sphere of diameter 22 μm (Rousseau *et al*., 2009).

It was found that as the separation between sphere and plane decrease, the relationship between heat flux per temperature and distance at tens of nano-meters approach a 1/*d* relation which is very close to the constant times $d^{-0.55}$ plus constant relation found by Narayanaswamy *et al* (2008). The result by Rousseau *et al*. (2009) is shown in Figure 2.14. This 1/d relation is drawn in the figure by dashed lines representing the asymptotes of the solid lines. The solid lines, which the data points follow, were calculated using Derganjuin Approximations (DA). DA solve the sphere and substrate

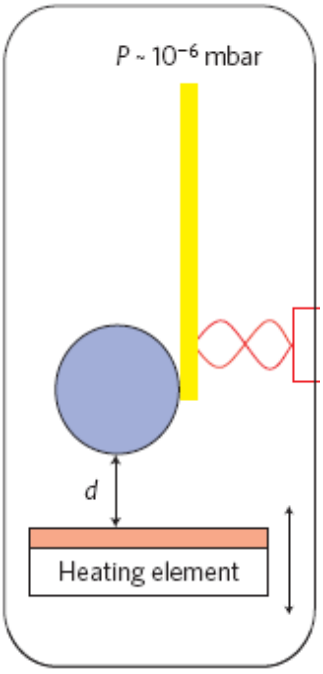

Figure 2.13. Experimental setup. (Rousseau, *et al*., 2009)

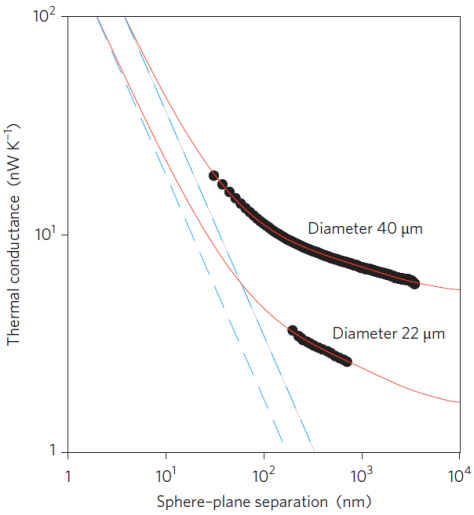

Figure 2.14. Experimental results (Rousseau, *et al*., 2009).

problem by integrating local contributions of heat flux using a heat transfer coefficient dependent on distance and temperature for two parallel planes. This approximation is illustrated in Figure 2.15 (Rousseau *et al*., 2009).

The enhancement of radiation transfer due to the interaction between surface phonon polaritons, or surface EM waves of ion fluctuations in polar materials and the tunneling of these waves from surface to surface with nanoscale gaps has been experimentally analyzed by Kittel *et al*. (2005) for the tip to surface geometry, and Rousseau *et al*. (2009) and Narayanaswamy *et al*. (2008) for the sphere to surface geometry. As shown in Figure 2.16, there are orders of magnitude difference between the gaps over which radiative heat transfer has been measured at differing geometries.

The most recent experimental study of near field heat transfer was conducted by Ottens *et al*. (2011). In this work, radiative heat transfer between 50x50x5 mm^3 sapphire

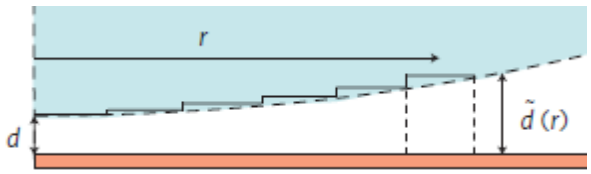

Figure 2.15 Visualization of Derganjuin Approximation (Rousseau *et al*., 2009)

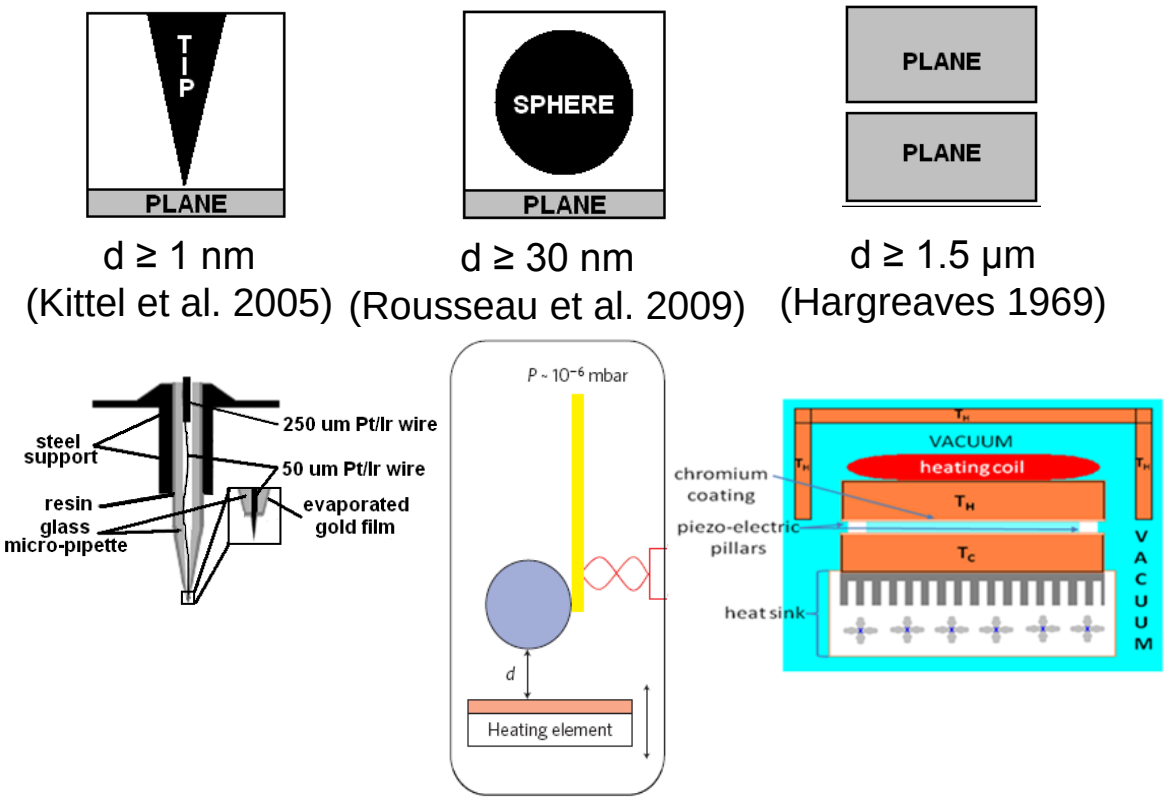

Figure 2.16. Minimum near-field measurement gaps at different geometries.

parallel plates was measured with variance in spacing between 2 – 100 μm. Four corners of the two near field heat transfer surfaces of the sapphire plates were coated with a 200 nm thick layer of sputtered copper. Capacitance across these copper coated corner areas was monitored for knowing and controlling plate separation and parallelism. A bi-axial mirror mount was utilized and controlled with stepper motors to equalize the four capacitances and bring the gap to different lengths to control the parallelism and adjust the height. Plate temperatures were monitored using silicon diode thermometers deposited on top of the top plate and bottom of the bottom plate. The experiment took place in an ultra-high vacuum ranging from $5x10^{-7}$ to $2x10^{-7}$ Torr. The colder temperature plate was kept at the environment temperature by radiating and conducting the heat received from the hot plate to the environment. The Macor spacer was attached to hot plate that thermally isolates it, while it is heated using a copper ring coil that was attached to the surface of the hot plate opposite the side adjacent to the cold plate. The setup is shown in Figure 2.17.

Although there was heat transfer from the hot plate to the environment, the only method of heat transfer changing in relation to the change in spacing had to be the near

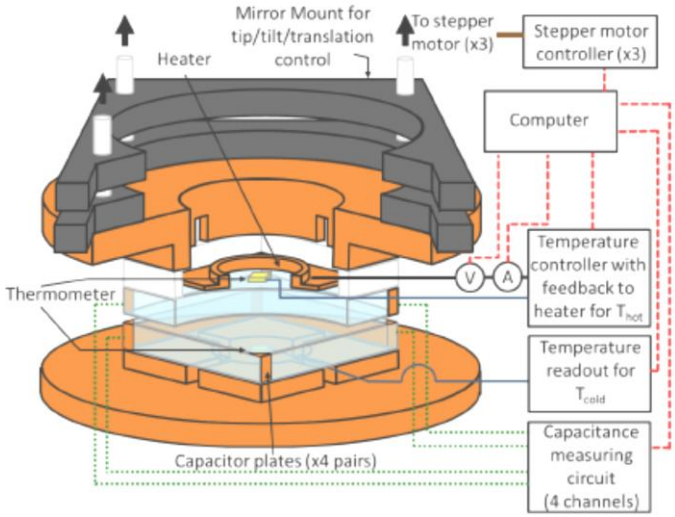

Figure 2.17. Experimental setup (Ottens *et al*., 2011).

field radiative heat transfer. Based on this, near field heat transfer effect was measurable and followed close to the predictions based on the theory from Polder and Van Hove as shown in Figure 2.18 (Ottens *et al*., 2011).

This study is unique in that it uses stepper motors and screws for positioning instead of using piezo-electric positioning. The deposition of 200 nm of copper on each surface limits the minimum gap size to above 400 nm. The displacement of the center in comparison with the perimeter was measured to be 170 ± 30 nm. Surface roughness was not mentioned in the paper. If there was roughness, then this would have an effect on

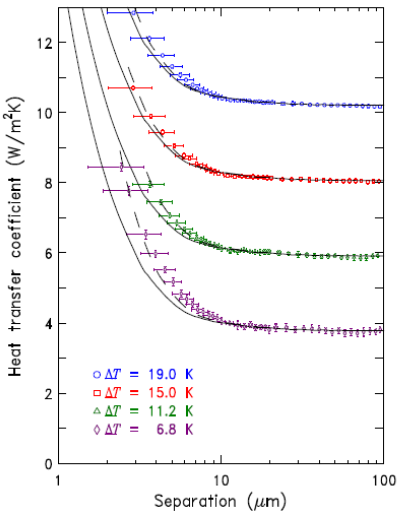

Figure 2.18. Experimental results (Ottens *et al*., 2011).

displacement uncertainty. The temperatures were measured 5mm away from the near field heat transfer surface which means that a distribution in temperature throughout each plate was not considered.

The plane to plane geometry with nanoscale gaps has been theoretically analyzed by Francoeur *et al*. (2008) as shown in Chapter 1 and illustrated in Figure 1.7 to show a near-field enhancement in energy transfer rate due to the coupling of lattice waves at the surface of a dielectric material. These waves are known as surface phonon polaritons. This also showed an enhancement due to coupling of these waves across thin films. The other key characteristic of this transfer is the narrowing of the spectrum of the energy transferred from surface to surface. These findings however need to be validated experimentally for plate to plate geometry not only in magnitude of flux, but also in terms of the frequency of the energy transferred, so that it can be applied in TPV devices. Challenges in measuring the near field enhancement of radiation include maintaining a uniform gap between parallel plates, maintaining a steady state flux and accurately and non-invasively measuring the temperature.

3. EXPERIMENTAL CONCEPTS

3.1. Problem Statement

This thesis aims to establish an experimental system that can be used for near-field radiation transfer measurements. Such measurements can eventually be used to validate the theoretical findings of many other researchers, including those by Froncoeur *et al*. about surface phonon polariton coupling between parallel silicon carbide surfaces separated by nano-scale gaps. This thesis will have the first shot at quantifying the enhancement of radiation by SPhP coupling/tunneling and will expand the scope of experimental work done at nano-scale distances to the parallel plate geometry. Also, it will expand the work done at larger distances with parallel plates by showing the dependence of radiative heat transfer between parallel plates on plate separation distance at the nano-scale.

3.2. Expected Results

The expected relationship between total rate of heat transferred between two plane-parallel planes, $q_{h\text{-}c}$, and separation distance, d, has been calculated in previous works. This geometry is shown in Figure 3.1. The formulation presented by Basu *et al*. (2009) which showed the relationship between total heat transfer and both d and dielectric constants. To calculate these results, it was shown that the total heat flux, $q_{h\text{-}c}$ is obtained by integrating the differences of the oscillatory functions, $\Theta(\nu,T_h)$ and $\Theta(\nu,T_c)$ multiplied by the weighing function $X(\nu)$ where T_h and T_c are the emitter and receiver plate temperatures, respectively (Equation 3.1). In this equation, each plate is assumed to be at uniform temperature, and ν is the frequency of light emitted radiatively.

$$q_{h-c} = \frac{1}{\pi^2}\int_0^\infty \left[\Theta(\nu,T_h) - \Theta(\nu,T_c)\right] X(\nu)\, d\nu \tag{3.1}$$

In practice, the integration is performed over the total range of frequencies of radiation that are above and below cut-off frequencies where the amount of radiation is negligible. The oscillatory functions are described by Equation 3.2, the Planck function.

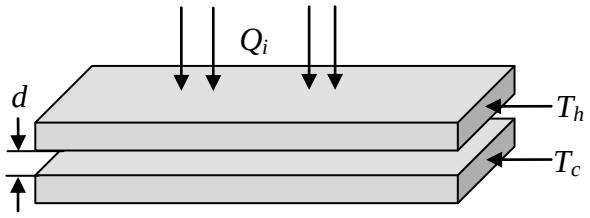

Figure 3.1. Experiment Geometry.

$$\Theta(\nu,T) = \frac{h\nu}{\exp\left(\frac{h\nu}{k_B T}\right)-1} \tag{3.2}$$

where h is Planck's constant, ν is frequency, k_B is the Boltzmann constant and T is temperature. Equation 3.3 is the weighing function, which integrates the frequency dependent exchange function over the possible wave frequencies.

$$X(\nu) = \frac{4}{d^2}\int_0^{\xi_c} \frac{\varepsilon''(\nu)^2 e^{-2\xi}\xi d\xi}{\left|(\varepsilon(\nu)+1)^2 - (\varepsilon(\nu)-1)^2 e^{-2\xi}\right|^2} \tag{3.3}$$

where d is the distance between plates and $\varepsilon(\nu)$ is the dielectric function and $\varepsilon''(\nu)$ is the imaginary part of the dielectric function.

$$\xi = \frac{\pi a}{a_c} \tag{3.4}$$

where a_c is the lattice constant, which is on the order of inter-atomic separation and ξ represents the d multiplied by the component of the wave vector that is tangent to the plates' surfaces. The maximum ξ over which the weighing function is integrated is ξ_c. By replacing a_c for a in Equation 3.4, it is found that ξ_c equals to π. The dielectric function must be calculated based on the properties of the material, in this case silicon dioxide. The real and imaginary dielectric constants for frequencies over the range of the peak emitted radiation from a black body at 300 K, were found in Palik (1998). This ranged from between the frequencies where radiation intensity was greater than or equal to 1% of the maximum emitted frequency, or the dominant frequency. This range was from 4.67 to

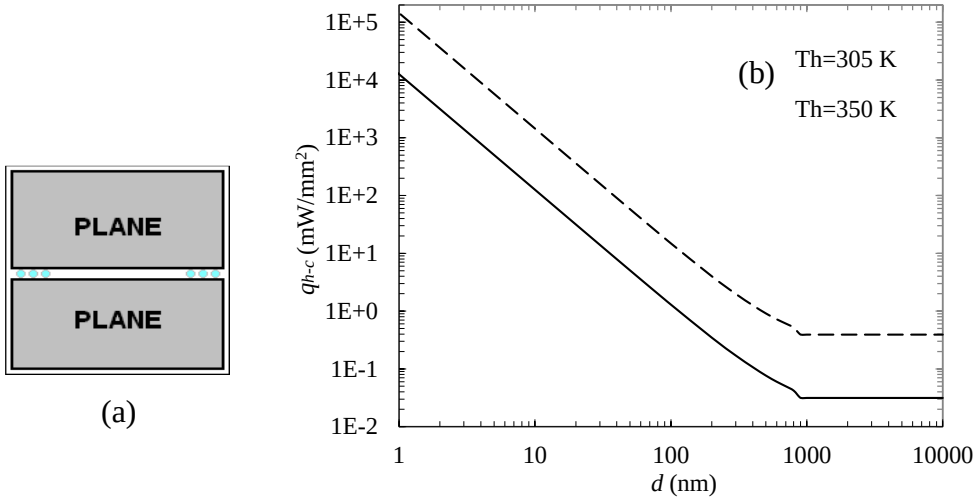

Figure 3.2. (a) Geometry of the parallel plates (b) Expected $q_{h\text{-}c}$ vs. d.

94.3 MHz.

The net radiative heat flux between two plane parallel silica plates, $q_{h\text{-}c}$, was calculated for distances, d, between plates varying from 1 nm to 10 µm. The geometry is shown in Figure 3.2a. The calculation is done for two cases. In both cases, T_c, the temperature of the colder plate, named the receiver is 300 K. The two cases are distinguished from each other by the hot plate or emitter temperature, T_h, which is 305 in one case and 350 K in the other. The results of these calculations are shown in Figure 3.2b.

This simulation, by showing the expected amount of heat transfer at given distances provides a design tool showing the amount of emitter heating capacity and receiver cooling capacity required to measure the heat transfer between parallel silicon-carbide plates at different nano-scale gaps. To put these calculations in perspective, a comparison with far field radiative heat transfer between parallel planes is done using, the equation for far field radiation between two plates in Equation 3.5.

In Figure 3.2b, at plate gaps of 900nm and above, the heat transfer is constant and unrelated to distance between plates, showing that this can be attributed to far-field radiation.

$$q_{h-c} = \frac{\sigma(T_h^4 - T_c^4)}{\frac{1}{\varepsilon_h} + \frac{1}{\varepsilon_c} - 1} \tag{3.5}$$

The radiative flux exchanged between two plane parallel surfaces with temperatures: T_h and T_c, and emissivities ε_h and ε_c, where σ is the Stefan-Boltzmann constant (Howell *et al*., 2011). To get a general idea though about net far-field radiative heat transfer, the emissivity of SiO_2 at temperatures between 300 and 350 K have been measured at around 0.25 (Han *et al*., 2005). The far-field radiative flux was calculated to be 0.34 and 0.027 mW/mm^2 for emitter temperatures of 350 and 305 K respectively which are consistent with the portion of the graph in Figure 3.2b with *d* above 900 nm. These values are orders of magnitude below the flux calculated as shown in Figure 3.2 for the near field.

3.3. Setup and Methodology

In order to measure the heat flux across a nano-scale vacuum gap at known temperatures an experimental setup in general must consist of: a heat source, heat sink, flux measurement, temperature measurement, and a sample with nano-spaced plates interspaced by a vacuum. Each part is given a sub-section. A generic setup, including a laser heat source focused on a sample using an optical train, power meter flux measurement, data acquisition, power supply, and their relation to the test sample, is shown in Figure 3.3.

3.3.1. Sample Design

There are a few options for the sample or part of the setup where the radiative heat transfer occurs. The sample consists of two plane-parallel silicon plates coated with a thin film of silica. The variation of total radiative flux with plate separation distance must be measured, to validate the results presented in Francoeur *et al*. (2010). This can be accomplished either using multiple samples of parallel plates, each with a different separation distance that can be measured independently or a single sample with adjustable plate separation that can be measured at different separation distances. In any case,

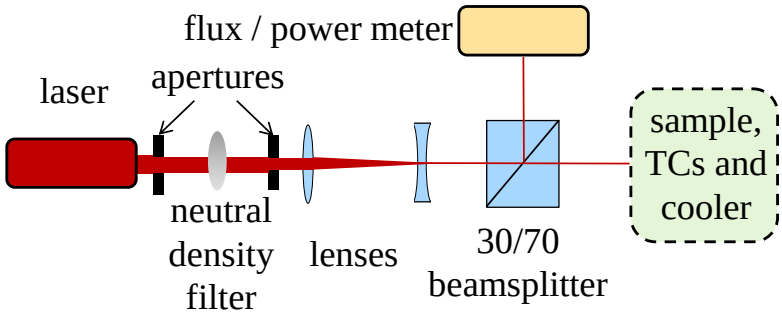

Figure 3.3. Experimental setup.

parallelism has to be maintained, conduction has to be minimal and the heat transfer must take place through a vacuum so radiation transfer is dominant and measurable. Depending on the sample design, the experiment might require a vacuum chamber and vacuum pump.

3.3.1.1 Option 1. The first option for sample design is a modular design. The samples, prepared separately, consist of two silicon substrates with SPhP supporting SiO_2 surfaces as shown in Figure 3.4. In this design, the samples are prepared in a near vacuum environment and the area between substrates is sealed to hold a vacuum between substrates. Different samples are fabricated each with a specific plate separation distance.

The advantages of this setup are that the flux measurement experiment can take place in an atmospheric pressure room at ambient temperature. The main disadvantage is high conduction due to the vacuum seals. Although the finished sample is sealed when plates

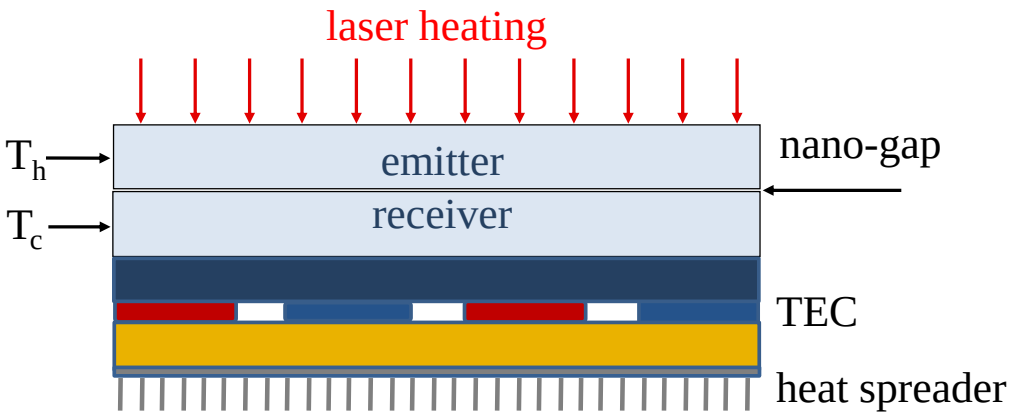

Figure 3.4. Option 1 sample and test setup design.

are bonded together, the sample's dimensions can be characterized before the bond and again after the heat transfer measurements are finished to double check parallelism. On the contrary verifying vacuum conditions is not possible, however if there is a leak, it should be noticed in terms of the magnitude of heat transfer, which would increase greatly if conduction through air is allowed between plates.

3.3.1.2 Option 2. The second option, motivated by the proven reliability of piezoelectric pillars, includes one sample with plate separation varying controllably based on the charge given to the piezoelectric pillars which raise and lower the emitter or heated plate as shown in Figure 3.5.

The piezoelectric pillars in Figure 3.5 are between the emitter and the thermo-electric cooler (TEC). Separation at large distances, or distances larger than wavelength of the laser may be measured using diffraction microscopy as shown in Figure 3.6. The piezo-electrics may be calibrated and when the plates come too close together to be measured using diffraction microscopy, or below the wavelength of the gap measurement laser, the distances between plates can be known.

The challenge of this setup is that it involves a technical measurement. The person measuring must learn how to control the piezo-electric pillars, working with the sample and all measurement devices in a vacuum chamber as well as precise placement of the reciever underneath the emitter once the piezo-electric pillars are calibrated.

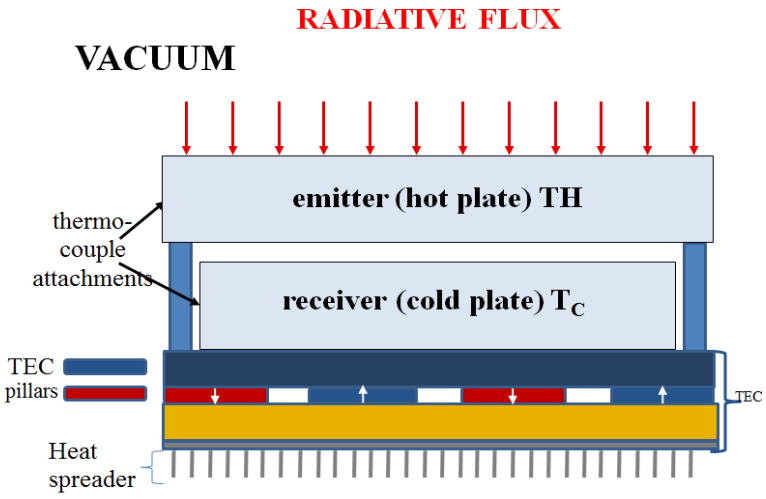

Figure 3.5. Option 2 test sample.

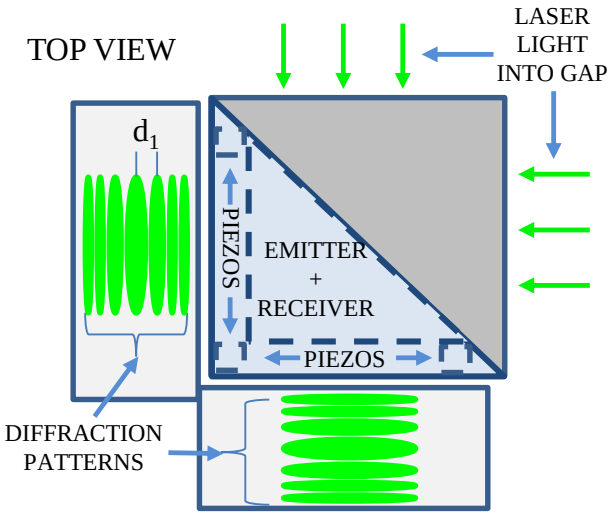

Figure 3.6. Diffraction microscopy (gap measurement).

3.3.1.3 Option 3. The third option is the only one which would not have silicon plates coated with silica thin films. This sample relies on lithography for vapor depositing two thermocouples across from each other at a nano-distance with a vacuum in between. The fabricated sample, shown in Figure 3.7, would be very different from the others in that the plates' areas would be very small. The step by step mask and vapor deposition that can be used for manufacturing the sample in Figure 3.7 is shown in Figure 3.8. The masks are shown on the middle of the top row and left of the bottom row, with exposure regions which expose the parts to be cured and subsequently removed (etched). After the degraded material from the UV or electron beam exposure is etched, two types of metals, the

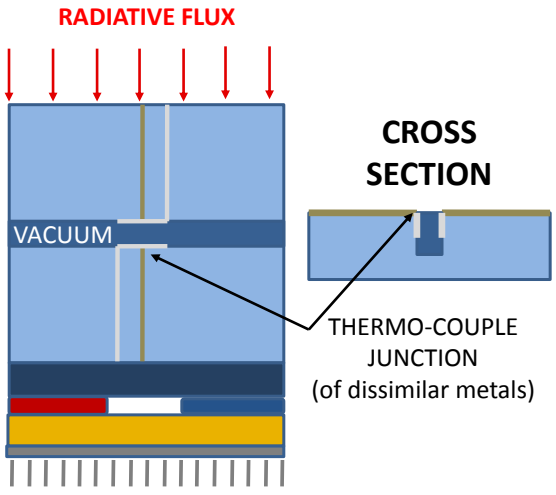

Figure 3.7. Option 3 test sample.

junctions of which make up the thermocouples, are deposited. The parallel plates over which the radiative heat transfer occurs are each made from one of the two metals. At the center of the parallel plates is the junction with the other metal as shown in the bottom right two drawings in Figure 3.8. The challenge of this setup would be isolating the measurement of heat flux across the thermal probes from the heat transfer from heated substrate to cooled substrate side which in this drawing are connected, so the measurement would rely heavily on modeling other pathways of heat transfer if not well mitigated. This method could be used with multiple sets of junctions as well.

3.3.2. Conduction, Bending and Strength Analyses for Sample Design.

The sample option chosen for this experiment was Option 1, the modular design, where individual samples are manufactured each with a different plate separation between the heated and cooled plates. Another parameter that can vary between samples is the wall and separator width. The wall that holds the vacuum between plates and holds the spacing is made of silica. The plates are made of silicon and the surfaces are coated with silicon dioxide. A combination of dry oxidation and etching is used to pattern silicon wafers with walls and silica surfaces.

The wafers are then fusion bonded together. After fusion bonding, the wafers are diced to obtain samples as is depicted in Figure 3.9.

The oxidation, patterning, etching and wafer dicing are carried out by Zafer Artvin and Tuba Okutucu from Middle East Technical University. The fusion bonding was

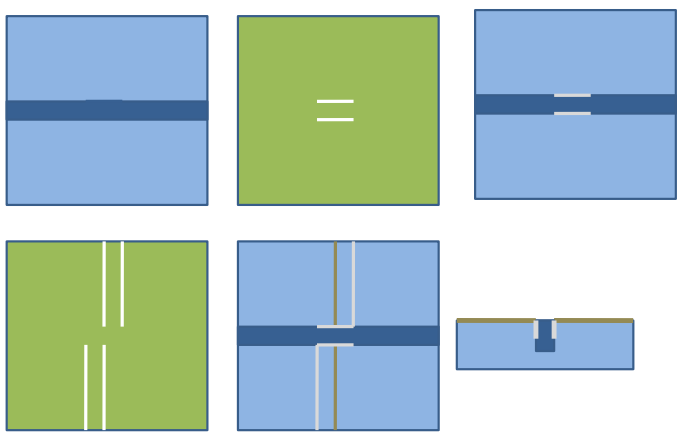

Figure 3.8. Mask and vapor deposition of thermo-couples.

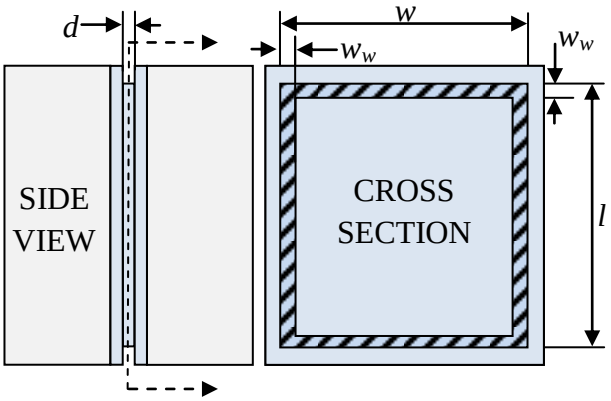

Figure 3.9. Sample design.

contracted to EV Group (EVG) of Austria. The sample design was based on fabrication limits, and resulting conduction vs. radiation rates and bending behavior. The goal of the conduction analysis was to find the best wall width and sample length to maximize the radiation to total heat transfer ratio.

The walls separate the plates at a given length and hold a vacuum between plates. Two cases are analyzed, where in both cases the ambient temperature and the receiver temperature, T_c, are 294 K. For the first case, the emitter temperature, T_h, is 344 K resulting in a ΔT of 50 K. In the second case, T_h is 299 K with a ΔT of 5K. Assuming temperatures through plates are uniform, flux values are calculated for samples considering the distance between plates.

Using the formulations presented in Section 3.2, the radiative heat transfer coefficient as a function of separation distance, $h_r(d)$, for SiO_2 –SiO_2, was calculated and the results are verified by solutions presented by Shen *et al*. (2009). This was calculated for a receiver temperature, T_c, of 300 K and emitter temperatures, T_h, of 305 and 350 K, to show that this linear approximation works for the range of ΔT that could be reasonably expected from this experiment. These results are presented in Figure 3.10, the total radiative heat transfer is represented in Equation 3.6.

$$Q_{rad} = (l - 2w_w)^2 h_r(d)\Delta T \tag{3.6}$$

where w_w is the wall width and l is the sample length shown in Figure 3.9.

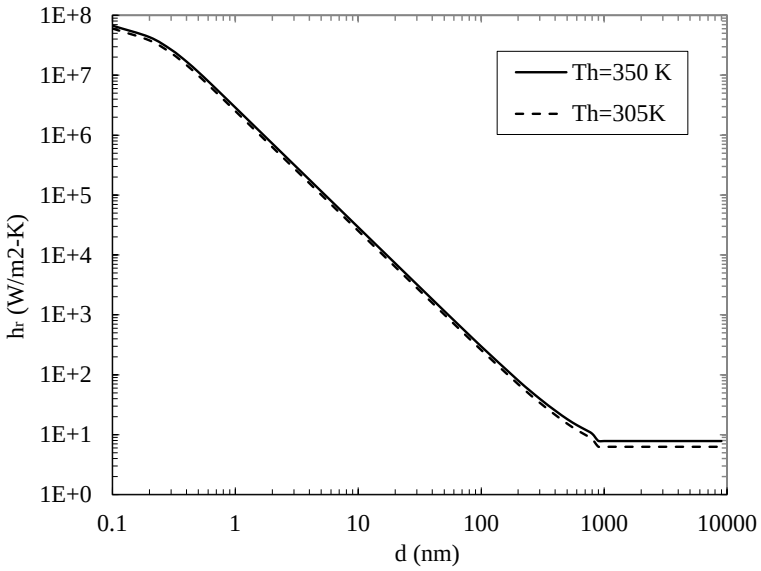

Figure 3.10. Change of radiative heat transfer coefficient with respect to gap for T_c of 300 K and T_h of 305 K and 350 K.

The total conduction through the walls, $Q_{cond,wall}$, separating plates is calculated using Equation 3.7.

$$Q_{cond,wall} = \frac{4w(l - w_w)k_{SiO2}\Delta T}{d} \tag{3.7}$$

where the thermal conductivity of polycrystalline glass, k_{SiO2}, is 1.38 W/m-K (Arpaci *et al.*, 2000). Based on Equations 3.6 and 3.7, 1x1 mm^2 samples with different plate separation and wall widths are analyzed. Table 3.1 presents the total heat flux necessary from heat source to achieve a ΔT of 5 K. Table 3.2 presents the percentage of radiative transfer with respect to the total heat transmitted. The percent of radiative heat flux in this basic analysis is identical for any ΔT, as radiation is predicted based on a nearly linearly ΔT dependent coefficient. Since conduction, also has a linear dependence on ΔT, this approximation does not show a great advantage gained by increasing the ΔT from 5 to 50. The calculation is instead used to show the effects of wall width and plate separation on amount and percentage of radiative to total heat transfer from emitter to receiver. It must be noted that the minimum wall thickness was 1.2 μm due to fabrication limits of the masking and etching.

Table 3.1. Total heat flux depending on wall width and separation with ΔT of 5 K.

Wall Thickness (μm)	Separation (μm)			
	0.05	0.1	0.5	1
0.05	0.012	0.0049	7.9E-04	3.9E-04
0.5	0.074	0.036	0.0070	0.0035
1.2	0.17	0.084	0.017	0.0083
2	0.28	0.14	0.03	0.01
3	0.42	0.21	0.041	0.021
5	0.69	0.34	0.069	0.034
10	1.4	0.68	0.14	0.068
20	2.7	1.4	0.27	0.14

Since best case for the 1x1 mm^2 samples, have less than 3% heat transferred via radiation, an additional study is carried out to predict the sample size required, with different wall widths to achieve 10% and 20% percent radiation. The results are shown in Table 3.3. It should be noted that sample length and width are equal.

This study was done up to wall widths of 20 μm, because a 20 μm wall width is recommend to seal a vacuum between plates by EVG, the wafer bonding company. As can be seen in Table 3.4, a 20 μm wall width would require a sample of tens or hundreds of centimeters in length to have a significant amount of radiation. This is not possible to fabricate due to current limitations in silicon wafer manufacturing, Czochralski process used to make crystalline wafers, and available tools for wafer processing, oxidation, etching, dicing etc. Consequently every sample made may not seal a vacuum. EVG takes

Table 3.2. Predicted percentage of radiative heat flux.

Wall Thickness (μm)	Separation (μm)			
	0.05	0.1	0.5	1
0.05	42	30	13	13
1.2	2.9	1.8	0.60	0.60
3	1.2	0.71	0.24	0.24
5	0.71	0.43	0.14	0.14
10	0.35	0.21	0.070	0.070
20	0.17	0.10	0.034	0.034

Table 3.3. Necessary sample length (mm) to achieve 10 and 20% radiation.

Radiation	Gap (μm)	Wall Width (μm)					
		1.2	2	3	5	10	20
10%	0.05	19	32	48	80	160	320
	0.1	26	44	66	110	220	440
	0.5	72	120	180	300	600	1200
20%	0.05	38	64	96	160	320	640
	0.1	58	96	144	240	480	960
	0.5	168	280	420	700	1400	2800

thermal images of the wafers they bond though, so it will be visible which samples are sealed, and which samples are worth measuring.

In the conduction vs. radiation analysis, other sample designs were analyzed. To guide the design of other samples, a calculation showing the percentage of radiation with respect to the ratio of total area to wall area through which conduction may take place was done. The result of this calculation is shown in Figure 3.11.

According to Figure 3.11 the ratio of total area to pillar/wall area should be greater than 15,000:1, 35,000:1 and 93,000:1 for 10%, 20% and 40% radiative heat transfer respectively for the sample with *d* of 500 nm. To minimize the possibility of surface roughness creating contact between plates and to keep plate temperature as uniform as

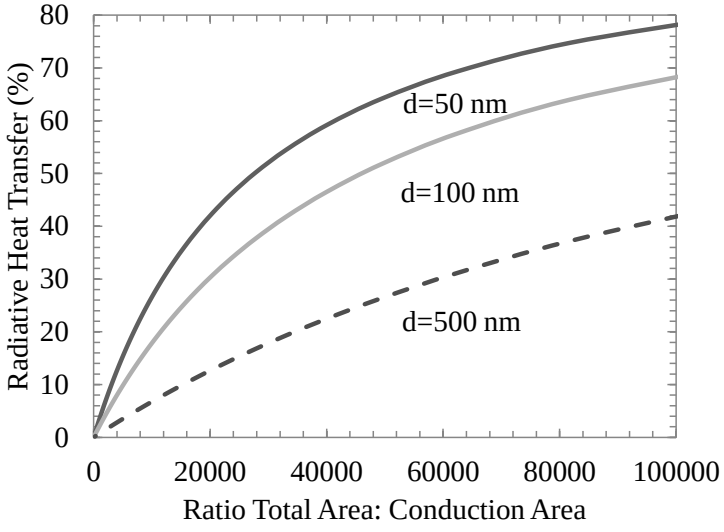

Figure 3.11. Radiative heat transfer percent vs. total area: conduction area.

possible, to allow external temperature measurement, samples' widths and lengths should be as small as possible. The minimum dice-able width/length for the samples is one millimeter due to limit of the device used for dicing samples from the wafer sandwich. If the calculation represented in Figure 3.11 is scaled down to a 1x1 mm^2 sample, the radiation percentage with pillar/wall area is as shown in Figure 3.12.

The pillar areas to achieve 10%, 20% and 40% radiative heat transfer for all samples with different gaps are 66.7, 28.6, and 10.8 μm^2 respectively. In addition to achieving a certain percentage with radiative heat transfer, bending of wafers as well as tangential strength of pillars are also considered. The bending analysis was done to ensure that plates would not make contact under atmospheric pressure. The tangential strength of the pillars was considered to ensure the sample could be measured on its side so it could be easily heated by a laser focused by lenses in an optical train.

For the bending calculation, the sample considered was the design that was studied in the thermal analysis with walls at the sample perimeter holding the plate separation on each of the four sides. To estimate the worst case, the boundary conditions considered were that of a simply supported plate where the displacement, *W*, and moment, *M*, at all

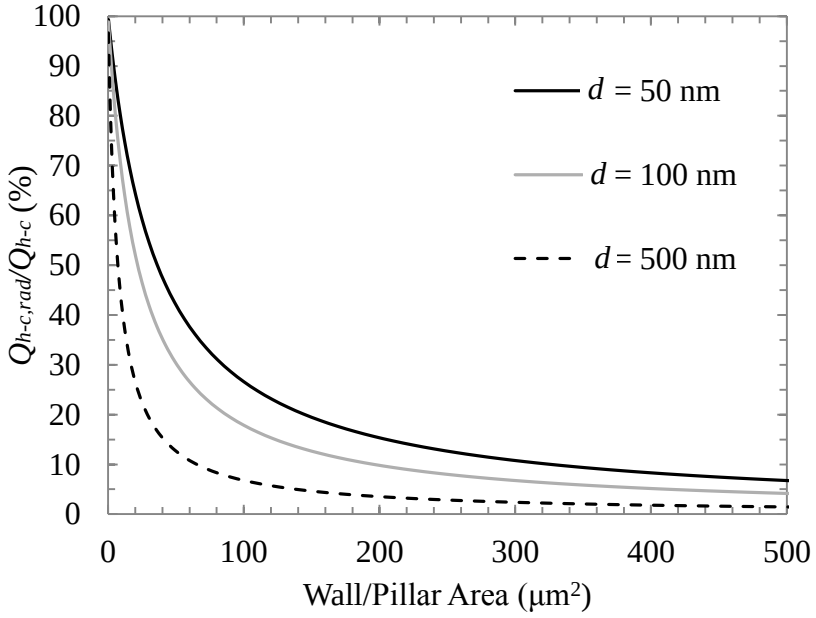

Figure 3.12. The change in radiative heat transfer percentage with total wall/pillar area of 1x1 mm^2 sample.

four edges were assumed to be zero. The equations representing maximum deflection, W_{max}, for a uniformly loaded plate can be presented as (Timoshenko *et al*., 1959)

$$W_{\max} = \alpha_{ra} \frac{pl^4}{D} \tag{3.8}$$

$$D = \frac{Eh^3}{12(1-\nu_p^2)} \tag{3.9}$$

Here α_{ra} is a numerical factor dependent on the ratio of length/width and for our square sample its value is 0.00406. Intensity of the distributed load, p for atmospheric pressure is $1x10^{-4}$ GPa. Since the sample is to be placed so that the plates are side by side, gravity does not increase or decrease the distributed load of atmospheric pressure on the plate surfaces. The constants, l, h and D, represent plate length, plate thickness and flexural rigidity, respectively. The modulus of elasticity for a (100) oriented crystalline silicon plate, E_{100}, is 170 GPa, and the Poisson's ratio, ν_p, is 0.064 (Hopcroft *et al*., 2010). The first bending analysis shown in Figure 3.13, presents the relationship between wafer thickness and bending. While the original wafer thickness is 500 μm, other wafer thicknesses could be achieved by thinning the wafer.

Since there are two plates, the gap between plates at the maximum deflection point

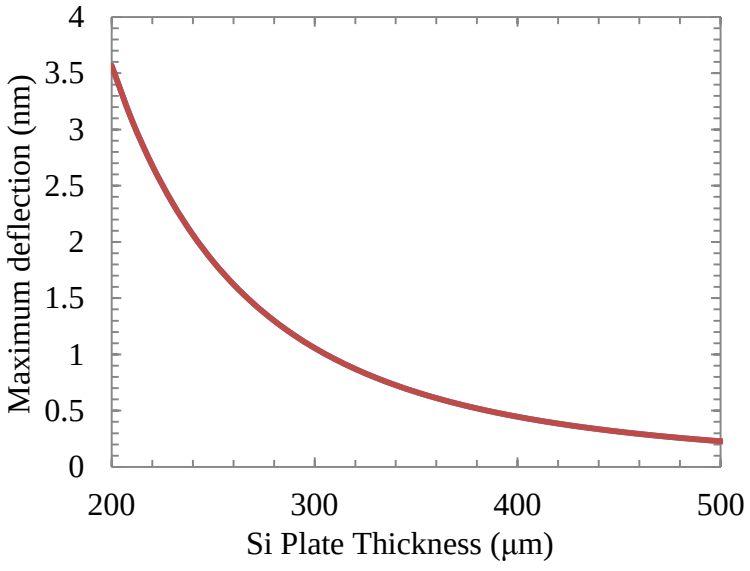

Figure 3.13. Deflection vs. Si-plate thickness.

will be reduced by twice the amount represented in Figure 3.13. Reducing the 1x1 mm^2 sample down to a thickness of 200 μm reduces the gap by 7 nm which in the case of a 50 nm gap sample reduces the gap by 13% at the point of highest deflection. Leaving the wafers at their original thickness keeps the gap reduction to below 1% at the point of highest deflection. This shows that thinning the wafer by significant amounts largely affects gap uniformity in the 50 nm gap case. As the slope exponentially decays in Figure 3.13 it can be seen that small changes in thickness that can be caused by oxidation and etching, on the order of hundreds of nanometers will not greatly affect the amount of deflection and gap uniformity.

The second variable looked at affecting uniformity in gap was sample length and width. Because larger samples may be required due to high heat conduction through walls, as the previous study showed requiring a 19x19 mm^2 sample with a 50 nm gap for 10% radiation, the relationship between bending or gap uniformity and sample length and width was tested. The result of this calculation relating length to bending is shown in Figure 3.14.

At a length and width of 19x19 mm^2, the silicon plate's maximum deflection is 12.7

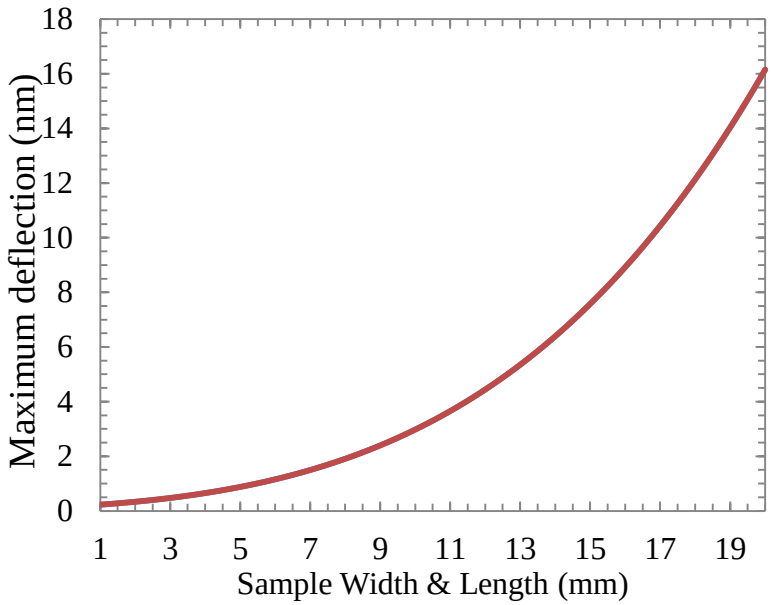

Figure 3.14. Maximum deflection of simply supported 0.5 mm thick Si-plate vs. *w*, where *w* and *l* are equivalent.

nm, so for the case where radiative transfer accounts for 10% of the total heat transfer, the plate maximum deflection causes a 50% change of the gap between plates. Although it would increase the conductive heat transfer from the hot to cool sides, a pillar can be placed in the center between plates, to reduce the plate deflection in one of the manufactured samples.

The last calculation done was to analyze the amount of pillar or wall area necessary to hold one of the plates tangentially. Shear stress is estimated using the average shear value τ_{ave} (Beer *et al*., 2011)

$$\tau_{ave} = \frac{P}{A_w} \tag{3.10}$$

where P is the load and A_w is the area of the wall which supports a silicon plate. Rearranging this, the minimum area of the silicon pillars or walls necessary to hold the adjacent silicon wafer is represented by Equation 3.11.

$$A_{w,\min} = \frac{P}{\tau_{\max}} = \frac{\forall_{Si}\rho_{Si}g}{\tau_{\max,SiO2}} \tag{3.11}$$

where ρ_{Si} is the density of silicon, $\forall_{Si}$ is the volume of the silicon wafer, g is gravity, and maximum shear strength of fused silica, $\tau_{max,SiO2}$ is 70 MPa (MolTech Gmbh, 2005). This expression is simplified by dividing $\forall_{Si}$ into its parts, area, A and thickness, t_{Si}. t_{Si} waslable 500 μm. The maximum ratio of A:A_w as was found by comparing conduction to radiative heat transfer as follows in Equation 3.12.

$$A : A_w = \frac{A}{A_w} : 1 = \frac{\tau_{\max,SiO2}}{t_{Si}\rho_{Si}g} : 1 = 6200 : 1 \tag{3.12}$$

The A:A_w ratio presented is for a factor of safety of one based on the maximum shear strength of SiO_2. If the sample instead is oriented during the experiment with one plate atop the other, the compressive strength of silica is 1.1 GPa, which allows the area of the silicon wafer to be 975000 times greater than the area of the walls or supports. If the wafer

thinning procedure is done, these numbers will be greater allowing for less conduction area. The drawback of thinning the wafer as discussed in the heating section is that it limits the wavelengths that can be used for heating the sample due to skin depth or the depth at which only 1% of the light transmitted through the surface is transmitted at a given wavelength. Regardless, there is a great advantage in orienting the sample so one plate sits atop the pillars or walls of the other in terms of minimizing pillar area or area through which conduction occurs. A safety factor of ten in this orientation would allow for over 40% calculated radiation in the sample with a gap of 500 nm and over 75% calculated radiation in the sample with a gap of 50 nm according to the calculation shown in Figure 3.11. The drawback of this design is that there wouldn't be enough pillars to enclose a vacuum within a 1x1 mm^2 sample, so the experiment would have to take place in a vacuum chamber. For enclosing a vacuum within the gap of a 1x1 mm^2 sample with the limit of 1.2 μm wall widths, the predicted ratio total area to conduction (wall) area is 209:1. This means that if the experiment is to take place at ambient conditions, with a 1x1 mm^2 sample, the sample may be oriented on its side with a shear strength factor of safety over 29.

The last thing to consider is that during the etching process, wall width at the point to contact the other plate is less than the design width because the etchant removes the wall corners as shown in Figure 3.15. This is not a predictable phenomenon and is based on etch time, so its profile can be measured after it is etched. This phenomenon should help reduce conduction between plates. Taking into account these calculations, sample designs were suggested, not only for measuring the radiative heat transfer, but also for quantifying the contact area and amount of conduction heat transfer in each sample. This was needed due to unknown effects of the exactness or tolerances of the masking, etching and bonding processes. The general design of these samples are shown in Figure 3.16a, b and c. Three different sample types: A, B, and C were considered as part of the same sample design and fabrication. Ideally all samples described here could be made and tested, but for our purposes, testing at ambient pressure and temperature sample style A was fabricated and tested. All three sample styles and different dimensions for an ideal case where many more samples could be manufactured and tested in different environments, but using the same sample manufacturing techniques, are listed in Table 3.4. Dimensions of the samples are listed at the top and side, checkmarks are put where the dimensions at the side and top

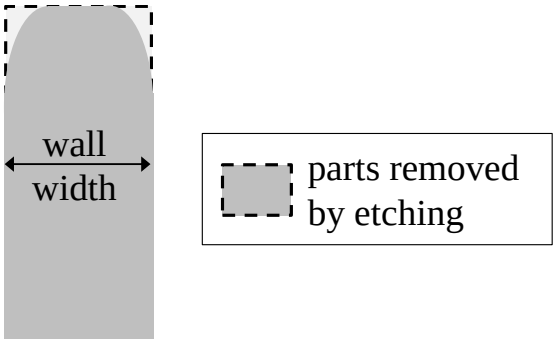

Figure 3.15. Effect of etching process on wall width.

correspond to a sample to be made. In sample C, there are more than two varying parameters, so instead of a checkmark, the value of the third varying dimension is written in the cell corresponding to the other two varying parameters. The factor of safety is listed in the middle of the table. Each factor of safety listed corresponds to that all the samples in its row. *d*, the space between plates is another varying parameter, but not mentioned in this table which guides the design directly affected by the masking process. *d* is uniform for all samples coming from a given wafer sandwich.

After the bonding process, the largest sample size holding a vacuum gap not collapsing during bonding was 2x2 mm^2. After wafer dicing, the measurable samples were 1x1 mm^2 with wall thicknesses of 2 and 3 μm with a gaps of 25, 50, 100, and 200 nanometers. To measure these samples with a ΔT of 5 K, if they held the vacuum condition, not counting the loss of conduction area due to the etching process, the 100 nm gap samples will require 0.14, and 0.21 W of heat input for the samples with wall widths of 2 and 3 μm, respectively. The percentage of predicted near field radiation heat transfer,

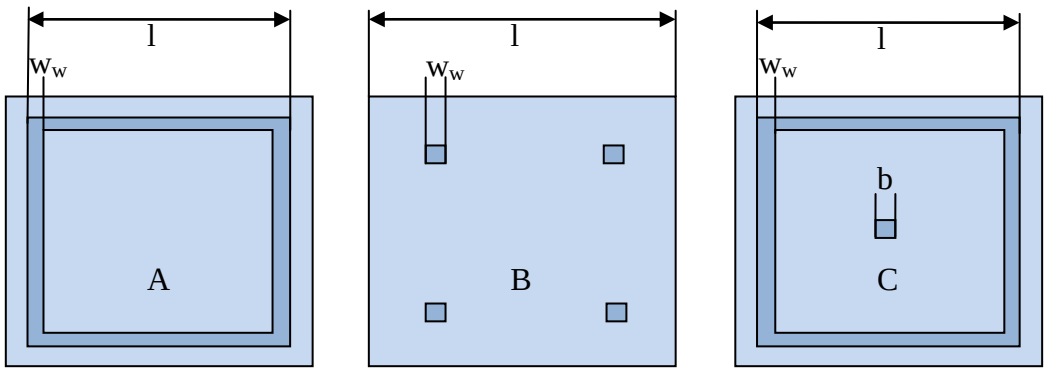

Figure 3.16. Sample design suggestions.

ignoring conductive surface lost, as shown in Figure 3.20, due to etching is 1.1% and 0.71% for the 100 nm gap sample with wall widths of 2 and 3 μm, respectively. Because this approximate calculation does not take the loss of pillar contact area due to the etching process or contact resistance into account, the percentage of radiative heat transfer should be higher in the experiment. In the experiment, contact resistance is characterized using samples with no gap.

3.3.3. Temperature Measurement

Temperature will be monitored using external type-K thermo-couples. By setting flux at different steady state values, matching heater and cooler fluxes, flux vs. temperature for each sample or each separation distance between emitter and receiver will be obtained. The temperature measurements will be made using 25 μm diameter, electrically insulated temperature probes from ANBE SMT Co. Each of the temperature probe tips are placed at the center of the top side of the emitter and receiver, measuring T_h and T_c respectively. These are held in place using an x-y-z variable stage micro-positioner and thermocouple fixture.

The fixture, shown in Figure 3.17a and b, has been custom fabricated to mount on the Thorlabs x-y-z variable stage micro-positioner. The fixture holds the thermocouples at the same height and the tips separation at 0.5 mm which is the distance between the centers of the emitter and receiver.

The fixture was made by cutting channels into one 5 mm plate and sandwiching the thermocouples between it and another plate with same dimensions but without channels. It is assumed that plate temperatures are uniform throughout each plate due to the high thermal conductivity of silicon. In 3D simulations of the experiment by Kazemi Khosroshahi (2012) this assumption was confirmed.

The accuracy of the temperature measurement is affected by the accuracy of the thermocouples and of the data acquisition unit. The accuracy specified for the Agilent 34970A data acquisition unit is 1°C between -100 and 600°C. (Agilent Technologies, 2009) At temperatures of 0-200°C, the ANBE SMT Type-K thermocouples and Omega

thermocouples used for this experiment are within the temperature uncertainty per special limits of error wire. Special limits of error specify that the error must be less than or equal to 1.1°C. (ASTM International, 2012) By taking the square root of the sum of the squares, the overall temperature measurement accuracy for an individual temperature measurement with this setup is 1.49 °C.

3.3.4. Heat Source

The heat source needed to provide a steady adjustable amount of heat as well as enough flux for a quantifiable difference between the temperatures of the nano-spaced hot and cold plates. Based on the simple calculations presented in the Section 3.3.1, the flux needed to achieve a ΔT of 5°C in the two manufactured samples, the 100 nm gap samples with wall widths of 2 and 3 μm was 140, and 210 mW of heat input for the samples respectively. To limit the number of variables, the flux source also had to provide a uniform flux over the heated side of the sample. The radiative flux source chosen for this experiment is a 660 - 680 nm wavelength (red), 190 mW laser Model RLF18130. The laser, sold as a high powered laser pen was inexpensive, $30, but required attaching coolers, a power supply and mounting the laser pointer in a custom machined aluminum box so it could be fastened to the optical table as shown in Figure 3.18. A light source of this wavelength is ideal for heating a silicon wafer. This is due to the high absorptivity and low absorption depth of silicon in this wavelength range as shown in Figure 3.19. Absorption depth is the depth at which a hundredth of the total incident light is absorbed. At a wavelength of 670 nm, the

Table 3.4. Sample dimension suggestions.

Sample A				Sample B			Sample C			
w_w (μm)	l (mm)			Factor of Safety (shear)	a (μm)	l (mm)	a (μm)	l (mm)		
	1	2	5			1		1	5	20
1.2	√	√	√	1	2	√	1.2	b=1, 4	b=1, 4	b=1, 4
2	√	√	√	2	2.8	√	1.2	b=2	b=2	b=2
3	√	-	-	3	3.5	√	3	b=1, 4	b=1, 4	b=1, 4
5	√	-	-	4	4	√	5	-	-	-
10	√	-	-	5	4.5	√	10	-	-	-
20	√	-	-	10	6.4	√	20	-	-	-

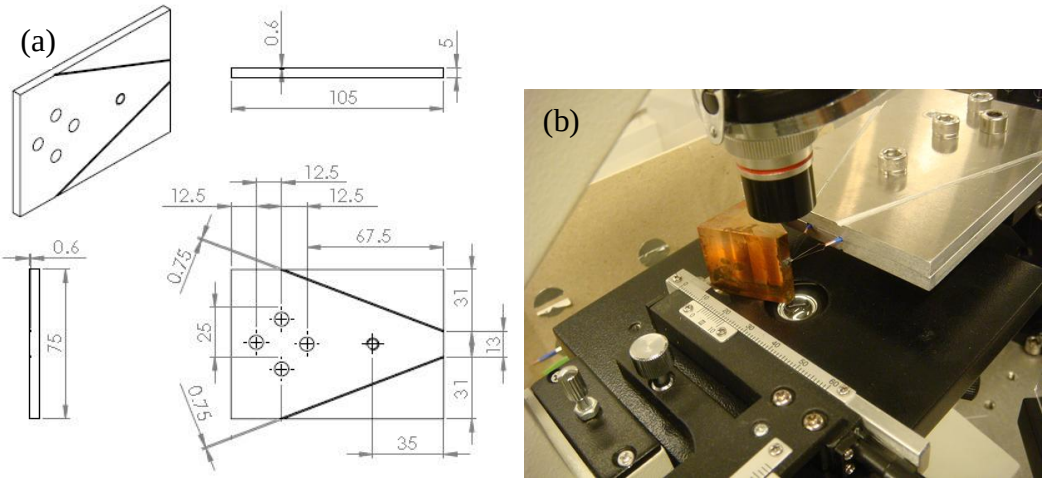

Figure 3.17 (a) TC fixture drawing (mm) (b) Fixture in use

absorptivity is less than 100 nm and absorptivity of greater than 0.5. The amount of the total laser light incident on the sample is controlled using an Edmond Optics™ 50 mm outer diameter circular variable neutral density filter model No. NT54-535, as shown in Figure 3.20. By varying the angle of the circular variable neutral density filter which the heating laser beam passes through, the portion total laser light passing through may be varied from 100% to 0% or 190 mW to 0 mW respectively.

To level the laser beam at the sample height, first the laser tip is brought to sample height. Using two mirrors each mounted on a biaxial mirror mount giving 4 degrees of freedom; the beam is leveled to the height of the sample. Leveling the beam is also necessary for directing the laser beam through the centers of the lenses that focus the laser.

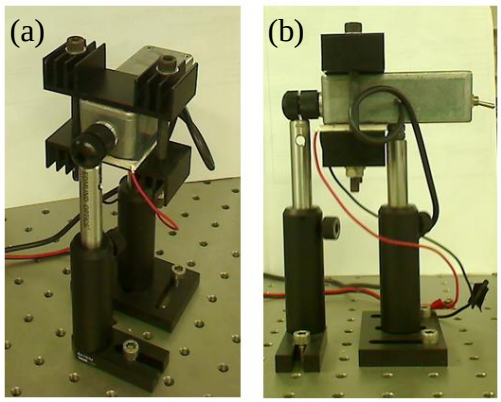

Figure 3.18. Laser (a) isometric view (b) side view.

The laser tip is screwed into an aluminum box which is cooled by a peltier cooler mounted on the bottom of the box as shown in Figure 3.18.

Below the peltier cooler and on top of the laser box, fins spread the heat generated by the laser and cooler's operation. The goal in using fins and peltier coolers is to achieve a steady operating temperature for the laser to keep a steady wavelength and power. The peltier cooler, driven at 1.5 V, was shown to bring the laser to steady temperature and output. Two apertures or diaphragms with centers at sample height are used in the beam leveling process. The diaphragms are later used to filter out the diffuse outer part of the beam so that a more uniform beam profile reaches the hot plate. One diaphragm is placed ahead of the neutral density filter, the other after the neutral density filter, just before the beam is focused.

The beam coming from the laser is divergent. After passing through the second aperture the beam first passes through a positive 50 mm focal length 1 inch diameter lens which focuses the beam, then passes through a negative 50 mm focal length lens to hold the beam at a constant diameter of 1 mm. The beam then passes through a 30/70 beam splitter, which reflects 30% of the beam to an optical power meter, described further in the

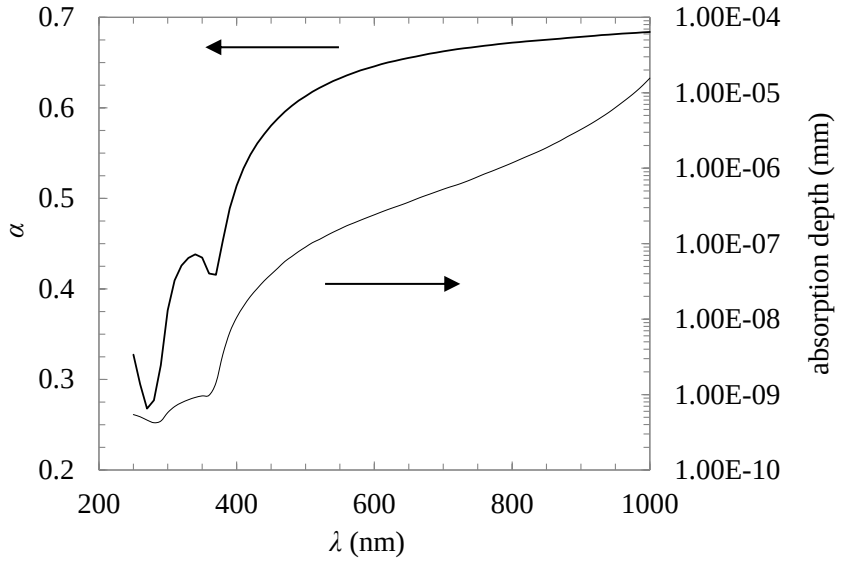

Figure 3.19. Si absorptivity and absorption depth vs. wavelength, (Green and Keevers, 1995).

Figure 3.20. Circular variable neutral density filter (Edmund Optics Inc., 2011).

Section 4.2. 70% of the beam is transmitted through the beam splitter and is incident upon the sample. To determine the amount of incident beam absorbed by the sample, a test is run at different beam intensities to determine absorptivity of the silicon used. This is described further in Chapter 4. The side of the sample where the light is incident is coated with silica. For the wafer sandwich with plate separation of 100 nm, the absorptivity was measured to be 0.76 ± 0.09. The wafer sandwich with plate separation of 200 nm has a measured absorptivity of 0.55 ± 0.05.

3.3.5. Sample Cooler

A Nextreme UPF4 Optocooler^{TM} thermoelectric cooler, (TEC) shown in Figure 3.21, along with a custom heat sink is used to cool the sample so that a steady state can be established. The TEC is a current controlled device which allows adjusting the cooling rate by limiting the current at a given voltage.

Maximum values are listed in terms of hot side temperature. Since our environmental temperature is around 25°C and minimum/maximum temperature

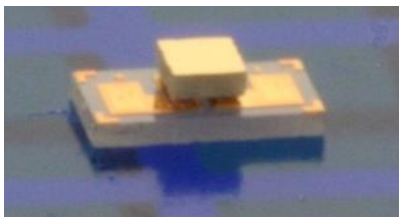

Figure 3.21. Nextreme UPF4 Optocooler ^{TM} thermoelectric cooler (1.5x2.5 mm^2 footprint) (NextremeThermal Solutions, 2009).

values are mentioned in Nextreme's data sheet for hot side are 85°C or 25°C, respectively. Values mentioned hereafter will be considered for a hot side temperature of 25°C. As suggested by Nextreme, ΔV_{MAX} or the maximum voltage, listed to be 0.20 V is applied to the TEC and it typically draws about half of the maximum current, I_{MAX}, that is 3.8 A. The maximum heat flux pumped by this device is 78 W/cm^2. Since the cold side is 0.74x0.74 mm^2, it is an ideal device to cool our 1x1 mm^2 samples because the entire surface of the cooler will be attached to the sample, so all the heat drawn through that surface will be coming from the sample. The drawbacks of this device are in the attachment process. The maximum temperature allowed for this TEC with wires attached is 120°C and the maximum temperature without wires attached is 150°C. The recommended solder, Indium Co.'s InSn solder's melting temperature is 118°C. Therefore, temperature has to be very carefully controlled during the attachment process and wires need to be held on to allow the solder to fully reflow. Due to these low temperature limits, the TEC itself used at reverse polarity cannot be used as a heat source for the soldering during the attachment of samples. Recently, a new TEC module (HV14) has been developed by Nextreme. The HV14 has the ability to operate at temperatures up to 150°C, which would allow it to be used as a heat source for soldering during the attachment of samples. The cold side is 1.48x1.0 mm^2 leaving some exposed area so all the heat pumped through the attached surface does not come from the sample, making it more difficult to accurately measure the flux coming out of the sample. However, this is not impossible since convection is predictable based on ambient temperature and the temperature of the cooler with some uncertainty. The maximum heat flux that can be pumped by the HV14 cooler is 95 W/cm^2.

The UPF4 opto-cooler TEC was planned to be used for this experiment. It was planned to be attached to a heat sink. Accordingly, a thermal analysis was done to design a heat sink with a low enough thermal resistance to dump all the heat pumped and generated by the UPF4 opto-cooler. Based on these calculations we understand the amount of heat transfer needed to be removed from the hot side of the sample in each case. For the worst, but measurable and manufacturable test sample, a gap of 100 nm and wall thickness of 3 μm, 208 mW needs to be removed at room temperature, or 294 K. Over 0.74x0.74 mm^2 surface, the heat flux that must be removed from the sample is 36.5 W/cm^2. Using the diagrams from Nextreme's UPF4 guide, the coefficient of performance (*COP*) with a ΔT of 5 K is estimated to be 2.25. The *COP* is defined as follows:

$$COP = -\frac{Q_{out,cond}}{P_e} \tag{3.13}$$

where $Q_{out,cond}$ is the heat into the cooler from the sample, and P_e is the electric power needed to drive the peltier-cooler. This means the required electrical power will be 92.4 mW. The Q_h that needs to be dumped by the peltier cooler is:

$$Q_h = P_e + Q_c \tag{3.14}$$

which gives 230.4 mW, so since T_h is five degrees above room temperature, T_∞, the required thermal resistance is calculated by Equation 3.15.

$$R_{\min} = \frac{T_h - T_\infty}{Q_h} \tag{3.15}$$

Therefore, the cooling solution for this setup needs to have a thermal resistance less than or equal to 21.7 K/W to remove the heat generated. Using, the temperature of the TEC cold and hot plates and performance diagrams, (Nextreme Thermal Solutions, 2009), the heat flux to be removed from the hot plate of the TEC was calculated. Using the temperatures of the emitter and receiver as well as the room temperature and the heat flux, the needed thermal resistance for the cooling solution is calculated.

A heat spreader is designed, which is used between the UPF4 TEC and the heat sink. The design was optimized for the minimum thermal resistance. Thermal resistance R_{th} was calculated by the following expression:

$$R_{th} = R_{sp} + R_{si} \tag{3.16}$$

Here R_{sp} and R_{si} respectively represent the spreader and sink thermal resistances.

$$R_{si} = \frac{T_{source} - T_{si}}{Q_{out,cond}} \tag{3.17}$$

T_{source} represents the area weighted average temperature of the spreader where it contacts the source of heat, in this case the thermo-electric cooler hot plate. T_{si} represents the area weighted average temperature of the spreader where it contacts the heat sink.

$$R_{si} = \frac{1}{h_{eq} A_{base}} = \frac{1}{\eta h_{sp} A_{si}} \tag{3.18}$$

where h_{sp} is the heat transfer coefficient of the spreader. h_{eq} is the equivalent heat transfer coefficient that when applied to the surface of the spreader, represents a cooler or spreader that would connect to that surface. The depth was varied from 20 to 53.85 mm. Even with the smallest heat spreader considered in this study of width 25 mm height 25 mm and depth of 20 mm, shown in Figure 3.22, the maximum thermal resistance of 21.7 K/W is satisfied with ease. A large spreader must be used for this experiment because the spreader also serves as a fixture for the sample during the measurement.

3.3.6. Flux Measurement

By knowing the total incident light, the fraction of light reflected as well as absorbed, the heat flux into the sample can be obtained. A fraction of the laser light beam, after being focused, is diverted into a laser power meter using a 30% reflected 70% transmitted beam splitter, as shown in Figure 3.3, to continuously monitor the flux. In order to ensure

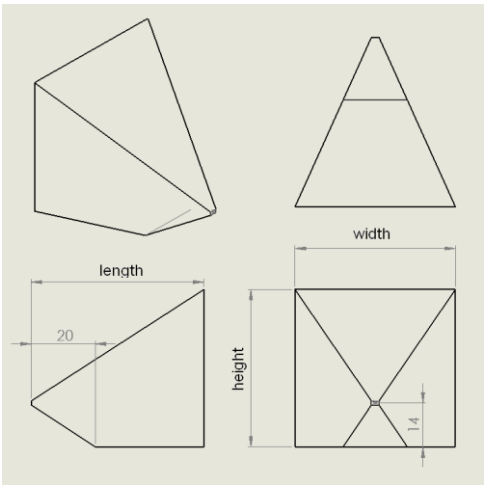

Figure 3.22. Heat spreader geometry.

stability of the laser source, in terms of power and wavelength, a 2.5x2.5 mm^2 surface area Peltier cooler will be connected to the laser head to keep the laser head at a steady operating temperature. Laser diodes heat during normal operation. A constantly monitored thermocouple will be used in conjunction with the Peltier cooler to keep the laser at a steady temperature throughout experiments.

The flux can be measured by two ways in the experimental setup. The first way is by diverting a known percentage of the laser beam which heats the sample to a Thorlabs S121C Photodiode Optical Power Sensor, which has a resolution of 10nW and a measurement uncertainty of ±3mW. (Thorlabs, 2012)

The second way to measure the flux is by measuring the flux coming out of the sample. The flux coming out of the sample will pass first through the cold side of the opto-cooler then through the pillars which move heat from the cold side to the hot side of the opto-cooler thermo-electric device as shown. In Figure 3.4, the heat flux vector points downward, and the sample's receiver is set on the cold plate of the cooler. If the temperature at the hot junction T_{hj}, temperature cold junction T_{cj} and the current I_l are monitored and the thermal conductance K_{in}, internal electrical resistance R_{in}, and overall Seebeck coefficient α_{pn} are known via prior calibration, flux may be determined using the following expression (Dalola, 2010):

$$q_{measured} = \alpha_{pn} T_{cj} I_l + K_{in}(T_{hj} - T_{cj}) + 0.5 I_l^2 R_{in} \tag{3.19}$$

The opto-cooler is controlled by the Agilent E3633A adjustable power supply (0-8 V, 20 A setting) based on performance curves provided by Nextreme that documents the change of voltage and current with COP.

4. MEASUREMENTS

Measurements are taken first to characterize the experimental setup to understand the relation between incident and the measured heat flux. Following that the surface absorptivities of the wafers from which samples were fabricated were characterized. Using the results of these characterization tests and direct sample measurements, total heat transfer between parallel plates was measured. All characterization measurements were averaged over 60 data points.

4.1. Setup Characterization

To identify the incident heat flux on the tested samples, it is necessary to characterize the setup. In each experiment, a portion of the laser beam used to heat the sample was diverted by a beam splitter to a power meter, and the portion transmitted through the beam splitter would heat the sample. Although, a beam splitter that reflects 30% to the power meter and transmits 70% of incident radiation to the sample was considered to be used for this originally, to increase the maximum heat flux incident on the sample, a glass microscope slide that diverted a lesser portion of the beam to a power meter was utilized instead. Both transmitted and reflected radiation were measured with the power meter then compared to understand the ratio of radiation incident on sample to measured radiation. It was found that the ratio is:

$$R = \frac{Q_i}{Q_{meas}} = 9.65 \tag{4.1}$$

Q_i represents laser heat incident on the sample and Q_{meas} is the amount of heat diverted by the beam splitter to the power meter during experiments. The value is the root mean square (RMS) of 60 measurements. The corresponding values for incident and measured heat are 67.98 and 7.05 mW, respectively with standard deviations of 1.74 and 0.13 mW, respectively. ThorLabs S120C photo-diode power sensor used to make this measurement has a measurement accuracy of ± 3% and the PM100USB power meter has an accuracy of ±0.2% (Thorlabs, 2012). Using the second power equation, the uncertainty

in R, ω_R, was calculated in to be 0.44. Calculation of the uncertainty intervals of R, and other measurements, are presented in Appendix A.

4.2. Absorptivity Measurement

The absorptivity, α, of samples from each wafer was measured by measuring the incident flux for a pure conduction sample and comparing it with the sum of the flux transferred out of the sample by conduction, convection and radiation. Conductive flux out of the sample was measured by attaching the sample to a uniform 1.1 mm diameter 2 cm long protrusion from a copper heat spreader as shown in Figure 4.1.

To attach thermocouples and the sample, heat was applied to the copper block from below using a cartridge heater held within the base of the aluminum fixture in Figure 4.1. Thermocouples were not successfully attached using InSn or PbSn flux, so thermocouples were adhered to the copper protrusion using aluminum tape. The thermocouples were spaced 15.5 mm for the absorptivity test. This spacing is denoted as Δx in Figure 4.2. The positions of the thermocouples were each individually measured with uncertainties, ω_{x1} and ω_{x2} of 0.05 mm. To prevent convection from the sides of the protrusion, aluminum coated

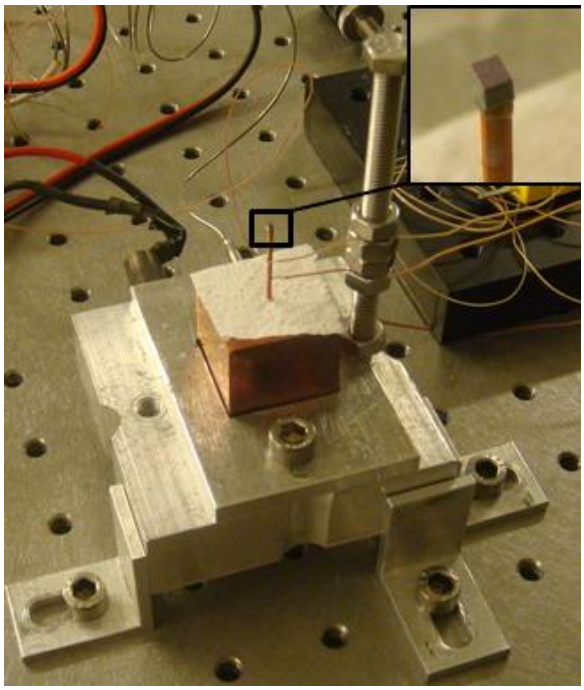

Figure 4.1. Flux measurement setup assembly.

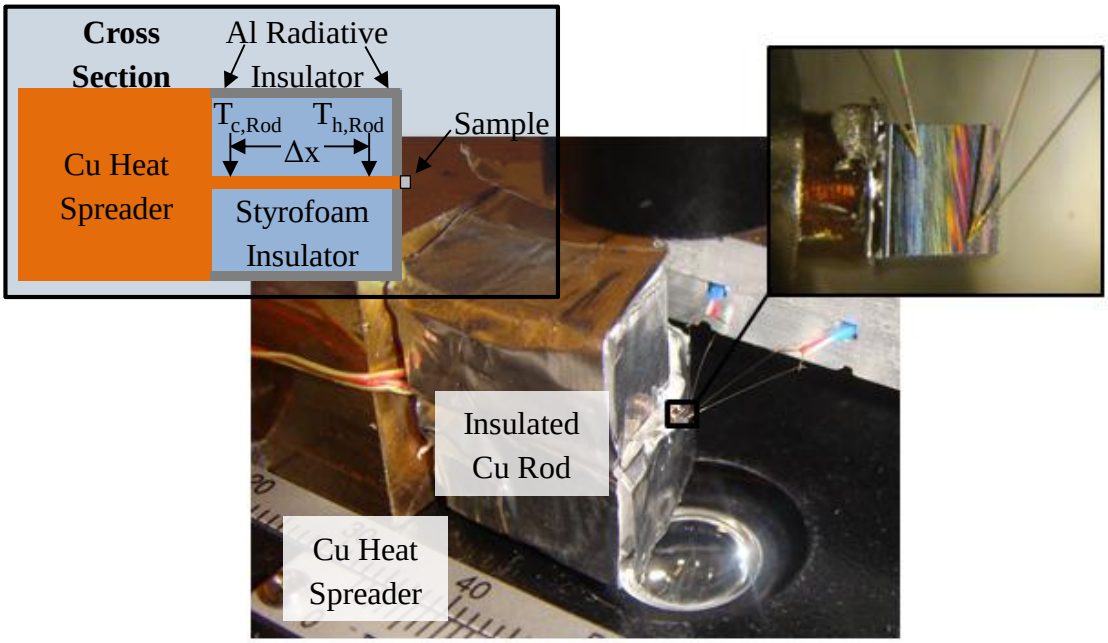

Figure 4.2. Flux measurement setup.

styrofoam was positioned around the copper protrusion as shown in Figure 4.2.

By applying the known incident laser heat Q_i while measuring T_h, T_c, $T_{amb,}$ and temperatures along the copper protrusion $T_{c,Rod}$, and $T_{h,Rod}$, for ΔT_{Rod}, α, the absorptivity of the heat provided by the laser was calculated by dividing the absorbed heat by the incident heat. At steady state, the total heat in and the total heat out of the sample are equivalent. The absorptivity is calculated in Equation 4.2.

$$\alpha = \frac{Q_{out,cond} + Q_{conv} + Q_{rad}}{Q_i} \tag{4.2}$$

where, $Q_{out,cond}$, the heat transferred conductively out of the sample via the copper protrusion is defined in Equation 4.3 by applying Fourier's Law.

$$Q_{out,cond} = -k_{C11000} A_{Rod} \frac{\Delta T_{Rod}}{\Delta x} \tag{4.3}$$

where k_{C11000} is the thermal conductivity of Copper 11000, which is 388 mW/mm-K. (Callister, 2007) $A_{Rod} \pm \omega_{\mathrm{ARod}}$, the cross sectional area of the protruding part of the copper

block is 0.950±0.086 mm^2. Δx is the distance along the protrusion between the thermocouples used to measure ΔT_{Rod} as shown in Figure 4.2. $\omega_{Qout,cond}$, the uncertainty of the heat transferred conductively out of the sample is calculated for each case using Equation A.5 in Appendix A. For the characterization relevant to the 100 nm gap samples, $\omega_{Qout,cond}$ was 70.85 mW and for the 200 nm samples was 70.05 mW. Convection losses to the environment can be defined as;

$$Q_{conv} = Q_{h,conv} + Q_{c,conv} = h_h A_h (T_h - T_\infty) + h_c A_c (T_c - T_\infty) \tag{4.4}$$

where $Q_{h,conv}$ and $Q_{c,conv}$ represent the heat transferred convectively to the environment from the hot and cold plates respectively. A_h and A_c are the respective areas of the hot and cold plates. h_h and h_c are the heat transfer coefficient of air, for the emitter and receiver respectively. T_h and T_c are the emitter and receiver temperatures and T_∞ is the temperature of the surroundings. Similarly, the radiative losses to the surroundings can be represented as;

$$Q_{rad} = Q_{h,rad} + Q_{h,rad} = \alpha_{Si}\sigma\left(A_c\left(T_c^4 - T_{wall}^4\right) + A_h\left(T_h^4 - T_{wall}^4\right)\right) \tag{4.5}$$

where T_{wall} is the temperature of the surrounding walls of plexiglas from which heat is radiatively transferred to and from the sample. T_{wall} is assumed to be equivalent to the ambient temperature, T_{amb}. $Q_{h,rad}$ represents the heat radiated from the hot plate to the environment. ϵ_{Si}, the emissivity of a silicon wafer, is estimated to be 0.7.

In Equations 4.4 and 4.5, A_h and A_c represent areas of the emitter and receiver respectively and they are defined in Equations 4.6 and 4.7.

$$A_h = wl + 2t(w + l) \tag{4.6}$$

$$A_c = 2t(w + l) \tag{4.7}$$

where l is the vertical length, t is plate thickness, and w is the horizontal width. For all

samples, t was 500 ± 3 μm. Width and length varied sample to sample. h_h and h_c, the heat transfer coefficients of air which were calculated individually for each sample based on its temperature and for the hot and cold plates depending on the percentage of vertical or horizontal (up-facing or down-facing) surface area.

$$h_h = \frac{(w+2t)lh_v + wth_{h,u} + wth_{h,d}}{A_h} \tag{4.8}$$

$$h_c = \frac{2lth_v + wth_{h,u} + wth_{h,d}}{A_c} \tag{4.9}$$

For the sake of simplicity, h_cA_c and h_hA_h and their uncertainties are directly calculated, so it is not necessary to divide then re-multiply by A_h and A_c when applying these to calculate convection and the uncertainty in convection.

For each of the sample surfaces, the heat transfer coefficients, as mentioned in Equations 4.8 and 4.9, are calculated in Equations 4.10 through 4.12 and their respective uncertainties are calculated in Appedix A in Equations A.11 through A.13. (Kothandaraman and Subramanyan, 1975) The free convective heat transfer coefficient for a vertical surface, with height l, is

$$h_v = 1.37\left(\frac{\Delta T_c}{l}\right)^{0.25}, \tag{4.10}$$

for an up facing surface is

$$h_{h,u} = 2.49\Delta T_c^{\,0.25} \tag{4.11}$$

and for a down facing surface is

$$h_{h,d} = 1.31\Delta T_c^{0.25} \tag{4.12}$$

where ΔT_c is defined as the difference between the plate and surrounding temperatures.

For wafer sandwich A, with samples of plate separation 100 nm, the absorptivity was measured to be 0.766 ± 0.915. For wafer sandwich B, with samples of plate separation 200 nm the measured absorptivity was 0.547 ± 1.478.

4.3. Thermal Resistance Measurement

Using values from the absorptivity test and the known thermal conductivities of silicon and silica, the total thermal contact resistance was calculated. Contact resistances exist at the silica thin-film to silicon wafer interfaces and at the silica thin-film to silica thin-film interface as shown in Figure 4.3.

In each sample there are one silica-silica and two silicon-silica interfaces. The total thermal contact resistance as a function of area was calculated in Equation 4.13.

$$J_{th} = A\frac{T_h - T_c}{Q_{h-c}} - \frac{t_{Si}}{k_{Si}} - \frac{t_{SiO2}}{k_{SiO2}} \tag{4.13}$$

where A is the cross sectional area. t_{Si} and t_{SiO2} are the total thicknesses of silicon and silica between thermocouples, $Q_{h\text{-}c}$ is the total heat transferred from the hot to cold plates through the silica thin-films, which at steady state is equivalent to the heat out of the cold

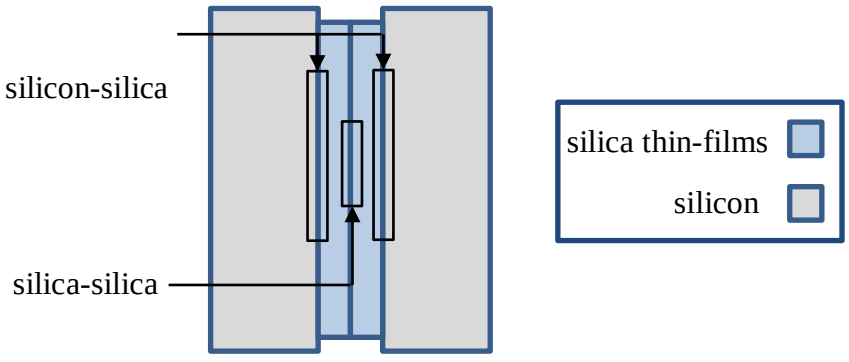

Figure 4.3. Sample interfaces with possible thermal contact resistance.

plate, $Q_{h\text{-}c}$ is calculated as:

$$Q_{h-c} = Q_{out,cond} + Q_{c,conv} + Q_{c,rad} \tag{4.14}$$

where $Q_{out,cond}$, $Q_{c,cond}$, and $Q_{c,rad}$ and their respective uncertainties are defined in Section 4.2. The uncertainty of $Q_{h\text{-}c}$ is calculated in Appendix A.

The total thermal contact resistance was assumed to be constant for each wafer sandwich from which samples were diced, so for each wafer sandwich one sample with no gap between surfaces was as used for total thermal resistance characterization. The values of thermal conductivity of silicon and silica are known with enough certainty that their uncertainty terms may be neglected.

J_{th} for Wafer A was calculated to be 0.00626 ± 0.01193 mW-mm^2/K. For Wafer B, J_{th} was calculated to be 0.00654 ± 0.00312 mW-mm^2/K. The prediction of uncertainty of thermal resistance is discussed and presented in detail in Appendix A. Given the measured total thermal resistance, different assumptions about the three thermal contact resistances that make up that total may be tested. The three approximations tested were: approximation one, 3 equivalent thermal contact resistances at each interface, approximation two, no thermal contact resistance at the silica-silica interface leaving two equivalent thermal contact resistances at the two silicon-silica interfaces and approximation three, a division between thermal resistances where 4/9 of the total was at each silicon-silica interface and 1/9 of the total was at the silica-silica interface. For the 200 nm and 100 nm samples, approximation one with all contact resistance at the silicon-silica interfaces yielded the most consistently physically meaningful results. These three cases are illustrated in Table 4.1. To calculate the different mechanisms of heat transfer across the nano-metric gap, which separates the hot and cold sample surfaces, first the surface temperatures are calculated, then, predictable forms of heat transfer, conduction through air and the silica walls was calculated. The remaining heat transferred from plate to plate is then attributed to heat transferred by near field radiative heat transfer or the coupling of surface phonon polaritons. To calculate surface temperatures, $T_{h,surf}$ and $T_{c,surf}$, the respective temperatures of the adjacent hot and cold wafer surfaces, the following relations were used:

Table 4.1 Assumptions for distribution of total thermal contact-resistance.

Assumption	Si-SiO_2 (hot-plate to thin-film)	SiO_2-SiO_2 (thin-film to thin-film)	Si-SiO_2 (cold-plate to thin-film)
1	1/2	0	1/2
2	4/9	1/9	4/9
3	1/3	1/3	1/3

$$T_{h,surf} = T_h - Q_{h-c}\left(\frac{J_{th}^{'} + \frac{t_{Si}}{k_{Si}} + \frac{t_{SiO2,h}}{k_{SiO2}}}{A}\right) \tag{4.15}$$

$$T_{c,surf} = T_c + Q_{h-c}\left(\frac{J_{th}^{'} + \frac{t_{Si}}{k_{Si}} + \frac{t_{SiO2,c}}{k_{SiO2}}}{A}\right) \tag{4.16}$$

For defining fluxes, J_{th}' in Equations 4.15 and 4.16 represents the per area contact resistance between the thin film and the hot plate and the thin-film and the cold plate respectively. The J_{th}' values depend on the assumption regarding the how the individual contact resistances sum to the total measured thermal contact resistances. t_{Si} is the distance between the thermocouple and the silicon-silica interface, taken as 0.25 ± 0.1 mm. The t_{SiO2} was taken to be the thin film thickness. t_{SiO2} for Wafer A, from which 100nm samples were diced, the $t_{SiO2,h}$ and $t_{SiO2,c}$ were 230 nm and 120 ± 5 nm respectively. From Wafer B, which the 200 nm gap samples were diced, $t_{SiO2,h}$ and $t_{SiO2,c}$ were 200 nm and 50 ± 5 nm respectively. The uncertainties of predicted surface temperatures are presented in Appendix A.

4.4. Flux Measurement

Once the setup's beam splitter's transmissivity and reflectivity ratio is characterized, the wafers' surface absorptivities are characterized, and the thermal contact resistances are characterized, flux measurements with known accuracy can be made and analyzed to determine the near-field radiative heat transfer between plane-parallel plates with nano-metric separation. The goal is to measure radiative heat transfer in relation to temperature to understand near-field enhancement of radiation. To do this, the experimental setup is designed to input heat to the sample, remove heat from the sample at steady state and monitor a sample's plate temperatures and incident heat flux.

By measuring different samples with different amounts of conduction, conduction from the hot to cold plates is separated from the flux through the nano-gap. The nano-gap ideally holds a vacuum condition through which heat is transferred significantly only by radiative heat transfer. By looking at the magnitude of heat transfer across the nano-gap, it can be determined whether there is conduction through air between the two surfaces. In order to know the heat flux through the sample gap, the laser flux incident on the sample surface, the absorption of that flux into the silicon wafer, the amount of heat dissipated to the environment by convection and radiation, and the amount of heat transferred conductively to the other wafer must be known. The expression is as follows:

$$Q_{h-c,rad} = Q_{h-c} - Q_{h-c,air} - Q_{h-c,wall} \tag{4.17}$$

where $Q_{h\text{-}c}$ is the heat transferred from the hot to cold plate and is calculated during experiments by Equation 4.18. A similar expression was defined for $Q_{h\text{-}c}$ for the wafer characterization test that was presented in Equation 4.14.

$$Q_{h-c} = Q_{abs} - Q_{h,conv} - Q_{h,rad} \tag{4.18}$$

$Q_{h\text{-}c,air}$ is the heat conducted through air from the hot plate to the cold plate. This is found via Fourier's Law:

$$Q_{h-c,air} = \frac{k_{air}(A - A_w)(T_{h,surf} - T_{c,surf})}{\Delta x} \tag{4.19}$$

where k_{air} is 2.635x10^{-2} ±5.27x10^{-4} mW/mm-K (Lemmon and Jacobsen, 2004) A is the total area and A_w is the wall area. The surface temperatures were calculated based on different thermal contact resistance assumptions as mentioned in Section 4.3. $Q_{h\text{-}c,wall}$ is also found by Fourier's law with an additional term representing the thermal contact resistance between the silica wall and the surface.

$$Q_{h-c,wall} = A_W \Delta T_{surf}\left(\frac{k_{SiO2}}{d} + \frac{1}{J_{th}}\right) \tag{4.20}$$

where J_{th} is the thermal contact resistance at the silica-silica interface which is dependent on the thermal contact resistance approximation. The uncertainty in $Q_{h\text{-}c,rad}$ notated as $\omega_{Qh\text{-}c,rad}$ can then be described based on Equation 4.17, and the formulation is presented in depth in Appendix A.

This result is discussed thoroughly in Chapter 5. The uncertainty of the values exceed the values for radiative heat transfer except for the case of no thermal resistance, which was calculated only as a reference, because a non-zero thermal resistance was measured for each wafer sandwich.

4.5. Sample Flux Measurement

The measurement is done at steady state with ΔT of around 0.5 K with a plate separation, d, of 100 nm, and 200 nm, the flux from plate to plate is varied between 0-60 mW/mm^2. The flux is made up of conductive flux across the pillars along with along with the near field radiative heat flux. Conduction and contact resistance is quantified using pure conduction samples. By comparing the samples of same gap size, but differently sized pillars, the amount of conduction and amount of near-field radiative heat transfer is discerned.

5. RESULTS AND DISCUSSION

The experimental setup was designed to measure the radiative heat transfer between two nano-spaced plane-parallel plates. By doing these measurements, the aim was to verify calculations of near-field enhanced radiative heat transfer due to surface phonon polariton coupling between adjacent silica thin film surfaces. Samples of plane-parallel silicon-oxide thin film coated silicon plates were measured using the setup developed. Using the measurements described in Chapter 4, the setup and samples were characterized so radiative heat transfer from plate to plate could be measured.

5.1. Measurement Results and Analysis

Measurements for 2 plate separation distances d and multiple ΔT were made. To analyze all tests to single out the relation of radiative heat transfer with respect to d, results for different ΔT experiments with a common d were averaged by calculating a ΔT independent radiative heat transfer coefficient, h_r, as was shown in Section 3.2. Using the ratio of expected radiative heat transfer to the heat transfer including conduction transfer through the walls which separated plates, the average radiative heat transfer is shown. These results and the expected results are shown in Figure 5.1. This shows that before any post processing, the measurements agree reasonably with the established predicted rate of radiative heat transfer and relationship of radiative heat transfer rate to plate separation distance for two plane parallel silica plates. To describe and analyze the measurements in more detail, the 100nm and 200nm gap sample measurements were plotted in Figure 5.2 and Figure 5.3.

Each of the data points shown represent the average of 60 consecutive measurements taken at 1 Hz. during steady state heat transfer. The calculated total heat transfer radiatively through the vacuum gap plus that transferred through the silica walls is represented by, Q_{vac}. The heat transfer if additionally there was conduction through air through the gap, Q_{air} was calculated as was the radiative heat transfer, Q_{rad}.

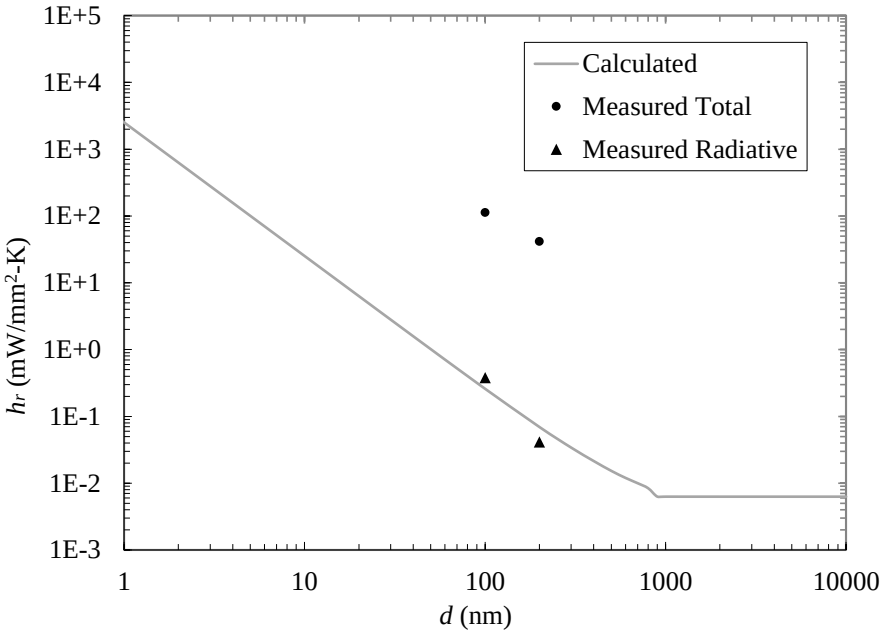

Figure 5.1. Measured and calculated total and radiative heat transfer coefficients vs. plate separation.

In Figure 5.2 and Figure 5.3, ΔT represents the difference between temperatures measured at the middle of both plates a short distance away from the adjacent surfaces over which the near-field radiative heat transfer occurs. For the calculated values though, each plate is assumed to have a uniform temperature. In reality the ΔT between measured points and the ΔT_{surf}, which directly is related to heat transfer, are different so in this analysis, this difference will be taken into account.

For the 200 nm gap sample measurements, the data points both follow the expected relationship between ΔT and $Q_{h\text{-}c}$, and lie below the curve for Q_{vac} as expected. To further test this result, using Equation 4.15 and Equation 4.16, the surface temperatures of the measured samples are calculated. The heat transfer vs. surface temperature for 200 nm plate separation is shown in Figure 5.4. This confirms that the heat transfer follows the expected radiative and conductive heat transfer between plates. This means a vacuum was held between plates by the sample. For the samples tested with plate separation of 100 nm, the results varied from the first to second sample, but as a general trend the points follow the expected relationship

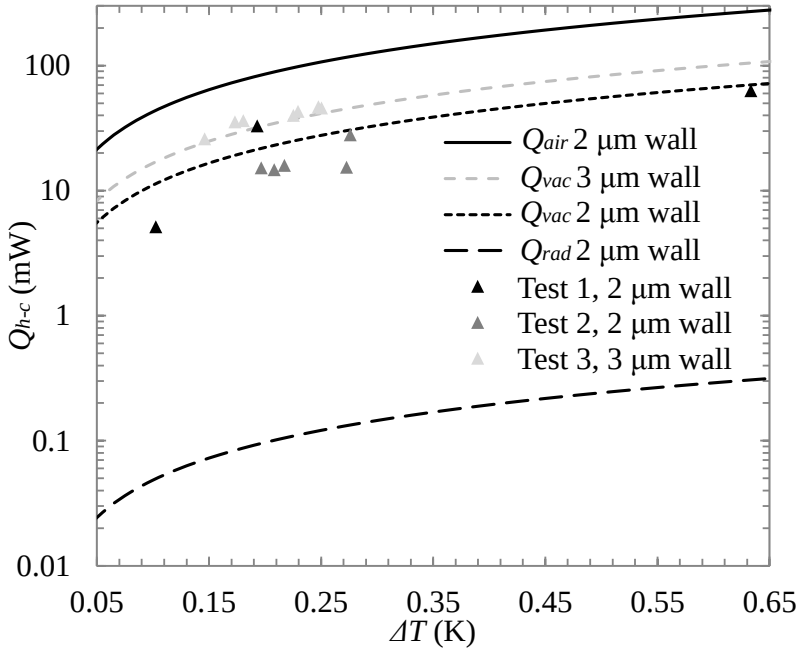

Figure 5.2. Total heat transfer vs. difference in measured temperatures. (d=100 nm) calculations for 2 and 3 μm wall thicknesses.

between ΔT and $Q_{h\text{-}c}$, and lie below the curves for Q_{vac} or Q_{air}. There were three test series. In each test series, conduction samples were characterized and 100 nm and 200 nm gap

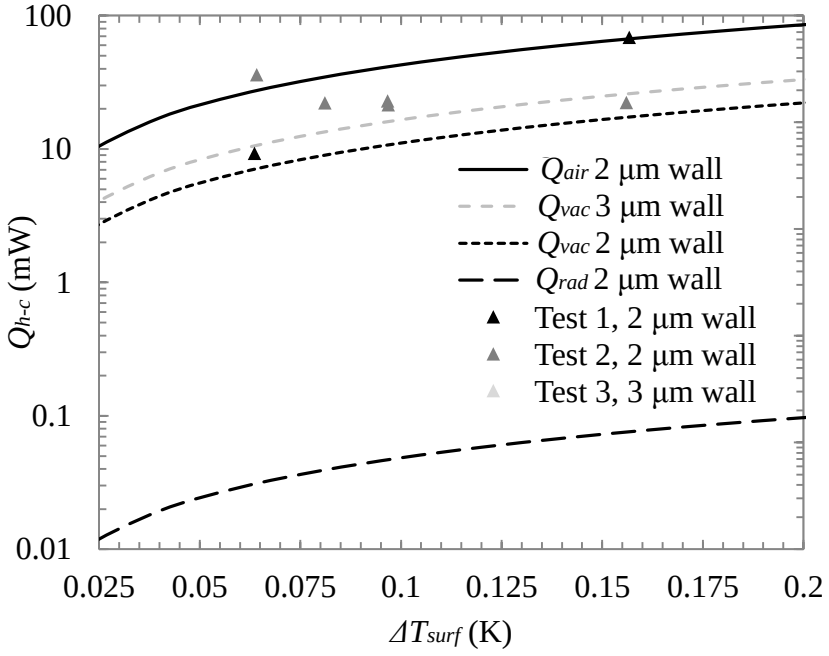

Figure 5.3. Heat transfer vs. calculated surface temperature difference (d = 100 nm) 2 and 3 μm wall thicknesses.

samples were tested. The first two test series were done using the same 100 nm sample and same 200 nm sample with one month in between test series. The third test series, done 2 months after the first test, was done with different samples from those used in the first two series, but all samples came from the same fabrication batch, each wafer sandwich corresponding to one plate separation distance. The samples with 200 nm plate separation, were of all the same dimensions. For the 100 nm sample though, the sample used in the third series had a wall width of 3 μm as opposed to the 2 μm walls in the sample used in the first two test series. In Figure 5.2, data points are split by wall width. Data points from test Series 1 and 2 lie below the curve for Q_{vac}. For the third test, the points lie on the curve for Q_{vac}. In this last series of tests, the thermocouple tips were placed much closer to the adjacent surfaces. This is evident in the post processing because if surface temperatures are calculated as if thermocouples were at the center of each plate, ΔT_{surf} is negative, which would violate the second law of thermodynamics.

For the first two test series, the data points are shown in black and dark gray in Figure 5.2. The points follow the expected relationship between ΔT and $Q_{h\text{-}c}$ and all but one lie below Q_{vac}. The results are plotted against the calculated surface temperatures in Figure 5.3. The calculation of temperature at the surface is highly dependent on the position of the thermo-couples. If the results vary greatly from test to test in a series, there is a strong possibility the thermocouple position was not consistent. For this calculation of surface temperature, one value for ΔT_{surf} was negative violating the second law, two of the values as shown in Figure 5.7 are around Q_{air}, and two are below the calculated value for Q_{vac}. These on the whole follow the expected $Q_{h\text{-}c}$ vs. ΔT_{surf} relationship.

Averaging the data with respect to the surface temperatures in all cases but for the sample with 3 μm wall thickness and a distance between plates, d, of 100 nm, the results are shown in Figure 5.6. The data from tests of the 200 nm gap sample agree with calculated results. The data from the 100 nm samples shows heat transfer higher than what is calculated for Q_{vac}.

As described in Chapter 4, the method measuring the radiative heat transfer was to first measure the total heat transferred between plates then breaking down the total into conduction through walls, conduction through air (if no vacuum was present) leaving the

remainder as a quantified total radiative heat transfer between plates. This calculation, due to the propagation of error, yielded uncertainties of magnitudes greater than the calculated values. For example, the calculated radiative heat transfer between plates spaced over 100 nm in for one test was found to be 9.23 ± 1064 mW. The measurement uncertainty is discussed further in Section 5.2.

This method required an assumption for how the measured total thermal-contact-resistance was distributed between the three interfaces as described in Section 4.3.

The calculation of surface temperatures critically depends on the thermal-contact-resistance as described in Equations 4.34 and 4.35. It also heavily depends on how the total measurable thermal-contact-resistance is assumed to be distributed between the three interfaces in each sample.

If thermal-contact-resistance at the Si-SiO2 interfaces was too low, the difference between plate temperatures, Tc,surf and Th,surf would be calculated high resulting in a calculation of Qh-c,wall and Qh-c,air in total would be greater than the total Qh-c, giving

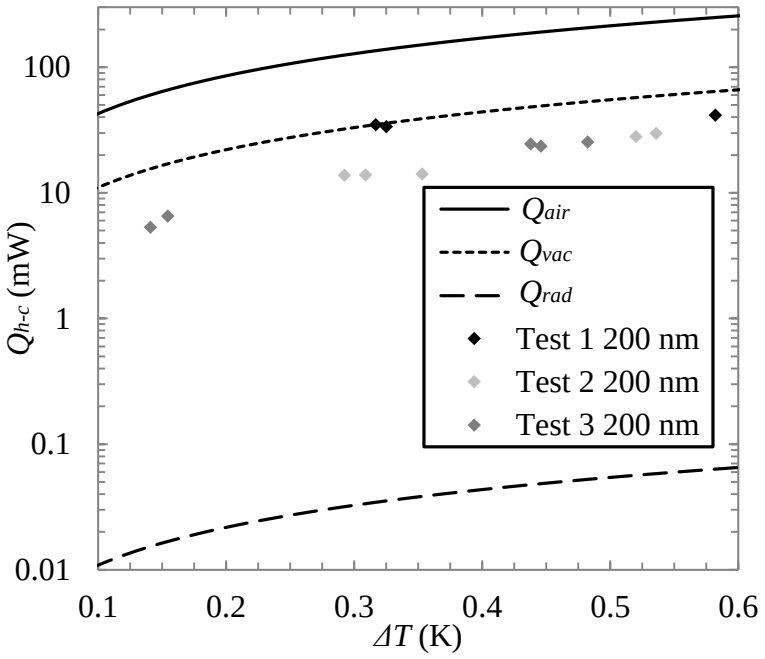

Figure 5.4. Total heat transfer vs. difference in measured temperatures (d=200 nm).

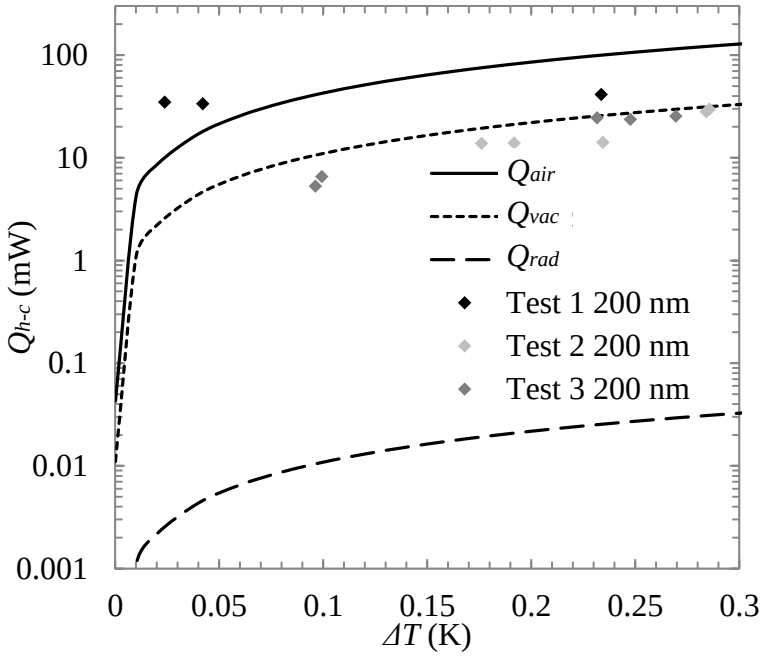

Figure 5.5. Heat transfer vs. calculated surface temperature difference for 200 nm plate separation.

negative results for the Q_{rad} calculations. If thermal contact resistance at Si-SiO_2 interfaces was too high, then the temperature difference between surfaces would be low, causing an

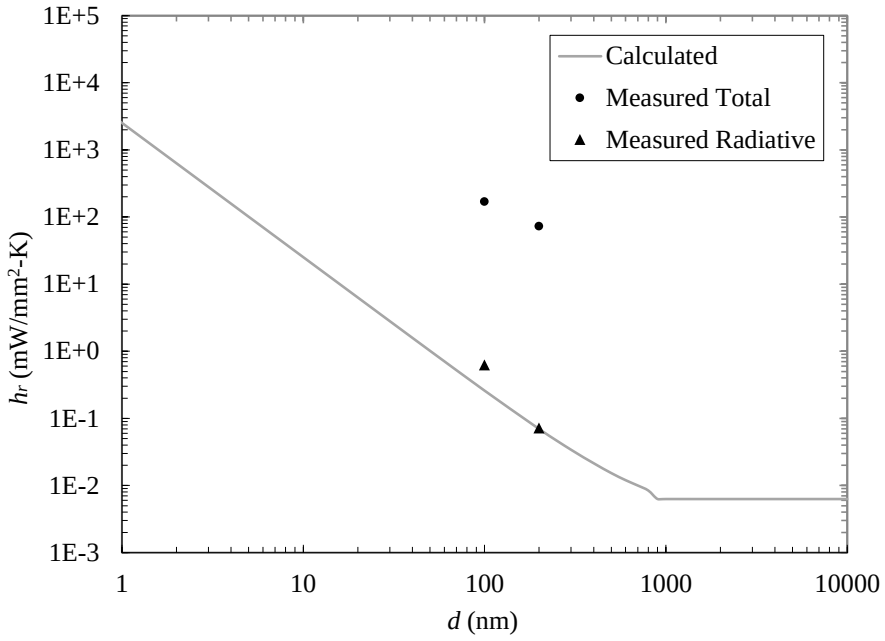

Figure 5.6. Measured data adjusted to surface temperatures.

undercalculation of the conduction through air and walls giving too high a value for the calculated radiative heat transfer. The different cases for J_{th}' are described in Section 3.2.

5.2. Uncertainty Analysis

Uncertainty in measurements were considered in this study using the general formula (Kline and McClintock, 1953):

$$\omega_r = \left[\left(\frac{\partial r}{\partial v_1} \omega_1 \right)^2 + \left(\frac{\partial r}{\partial v_2} \omega_2 \right)^2 + \cdots + \left(\frac{\partial r}{\partial v_n} \omega_n \right)^2 \right]^{\frac{1}{2}} \tag{5.1}$$

where r is the experimentally determined quantity that is predicted through measurements and $v_1, v_2, \ldots, v_n$ are the directly measured quantities r depends on. From thermocouple accuracy, to thermocouple positioning, positioning to flux measurement, all contributed to the final uncertainty in the measured heat transfer between plates.

Relative uncertainty in total heat transfer $Q_{h\text{-}c}$ for the 100 nm and 200 nm gap samples with respect to the measured temperature difference is shown in Figure 5.7. This indicates that the uncertainties of the measurements and the measurements themeselves are the same order of magnitude. For all measurements, $\omega_{Qh\text{-}c}$ is actually larger than $Q_{h\text{-}c}$. It

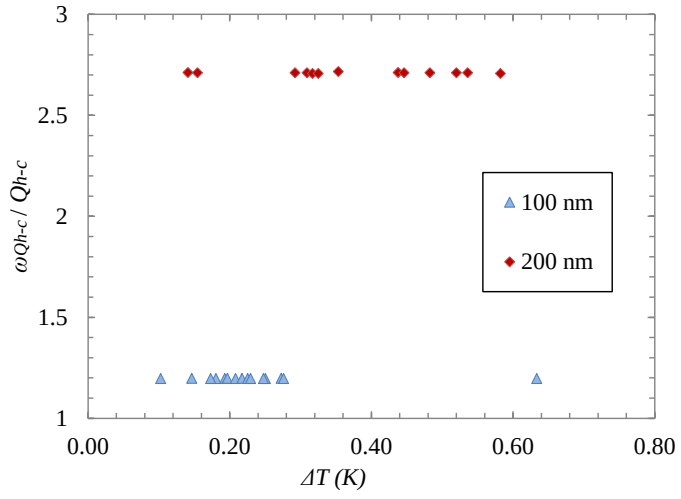

Figure 5.7. Relative uncertainty $\omega_{Qh\text{-}c}$ /$Q_{h\text{-}c}$ vs. ΔT.

is shown in Figure 5.7 that there is no dependence of the relative uncertainty in flux measurement with respect to ΔT. For all tests of samples with d of 100 nm, $\omega_{Qh\text{-}c}$ /$Q_{h\text{-}c}$ is 1.20. For the samples with d of 200 nm, $\omega_{Qh\text{-}c}$ /$Q_{h\text{-}c}$ is 2.71.

There are multiple reasons for the measurement uncertainty. Beginning with the heat flux and temperature measurement, the factors that increase uncertainty are analyzed and ways of reducing the total uncertainty are discussed.

Since value of concern is $Q_{h\text{-}c}$, it is necessary to consider how increasing incident heat flux affects the relative uncertainty of $Q_{h\text{-}c}$. Using the measured values of the experimental setup and the sample, $\omega_{Qh\text{-}c}$ /$Q_{h\text{-}c}$ was calculated for $Q_{h\text{-}c}$ ranging from 1 mW to 10 W. The relationship between heat flux and relative uncertainty of the measurement of heat flux is shown in Figure 5.8. This shows that by increasing the heat flux to 200 mW from the current average of 30 mW would reduce the relative uncertainty from 1.2 to 0.6.

Another important factor in the uncertainty of the flux measurement is the uncertainty of the temperature measurement. Thermocouple uncertainty plus that of the instrument is 1.49 K. For the ΔT measurement, the $\omega_{\Delta T}$ was 2.1 K which was greater than the difference between T_h and T_{cold} or ΔT for all of the experiments. This also affected the uncertainty of relative total heat transfer between plates due to its effect on the uncertainty

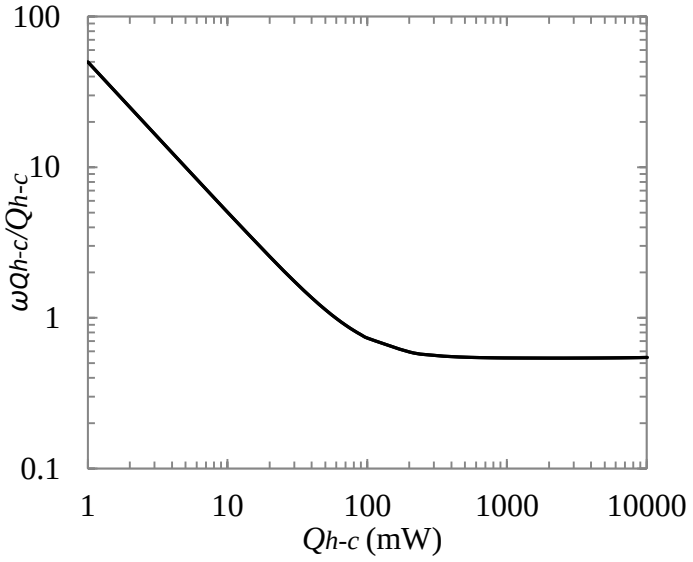

Figure 5.8. $\omega_{Qh\text{-}c}$ /$Q_{h\text{-}c}$ vs. $Q_{h\text{-}c}$ for current experimental setup.

of the sample absorptivity measurement. Since the temperature difference based on thermocouple separation uncertainty and the temperature difference between plates is linearly related to the incident heat flux, increasing heat incident on the sample would also reduce the effect the thermocouple positioning uncertainty has on the accuracy of the near-field radiative heat transfer calculation. The effects of increasing heat flux and using more accurate thermocouples, type T to ± 1.19 K and thermistors calibrated to ± 0.1 K are shown in Figure 5.9.

Thermocouple positioning for example although standardized by mounting thermocouples in a fixture attached to a micropositioner, there is still an uncertainty in the distance between thermocouples due to the flexibility and unequal curvature of any two thermocouple tips. The distance between thermocouples are 0.5 ± 0.1 mm. As the temperature difference at different points along the heat transfer direction are significant in relation to the difference in calculated surface temperatures, the effect of positioning uncertainty is significant. The solution to this positioning problem is to design a more precise method or tool for positioning the thermocouples. The position of the thermocouples during an experiment should be photographed through the microscope objective for each experiment so the location of each thermocouple can be taken into account during each calculation. Another uncertainty in the calculations of different forms of heat transfer was the uncertainty in sample dimension measurements. The thicknesses of the plates, the thin-films, the width and length of the plates as well as the wall widths of

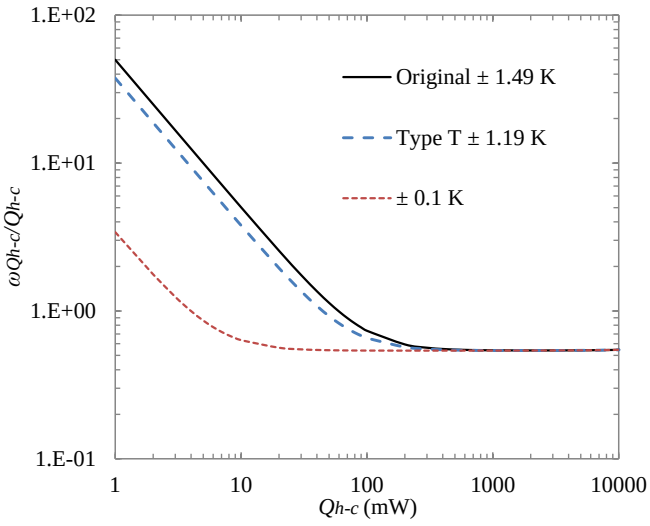

Figure 5.9. Effect of temperature measurement uncertainty on $\omega_{Qh\text{-}c}$ /$Q_{h\text{-}c}$.

the walls separating the plates all contributed to uncertainty in measuring the near-field radiative heat transfer between plates. This is shown in Figure 5.10. To improve this, all measurements of wall widths, and sample dimensions be done with a more accurate instrument such as a scanning electron microscope.

The accuracy of incident heat on the sample measurement is 3% of the measured value due to the accuracy of the photodiode power meter. Due to this limit in accuracy, no other flux calculations based on this measurement may have an uncertainty lower than 3%. This can be a problem especially in the case that radiative heat transfer is less than 3% of the total heat transfer, which would limit sample design. The accuracy of this device may be improved by calibrating it to a higher accuracy. The effect calibration to 1% accuracy would have is shown in Figure 5.10. To do this, a calibration beam at different intensities known and at the same wavelength and above and below the laser powers measured in the experiment This calibration beam would have to have an output of higher accuracy and precision than the power meter. Alternatively, the uniform copper rod, or protrusion from the copper block, used in the absorptivity measurement could be used directly to measure the flux out of the samples. The method of positioning of the thermocouples along the rod could be made more precise as could the measurement of the diameter of the rod. Main disadvantages of doing this would be the difficulty in sample attachment and the increased

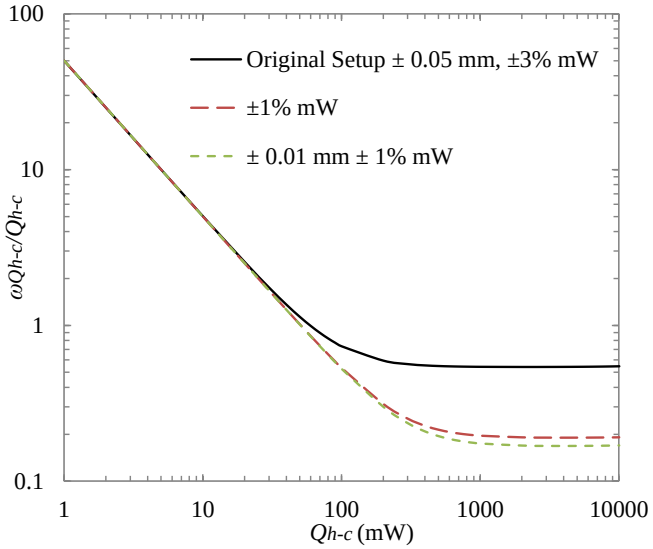

Figure 5.10. Effect of dimensional accuracy and flux measurement accuracy on $\omega_{Qh\text{-}c}$ /$Q_{h\text{-}c}$.

convective and radiative transfer to the environment due to a higher thermal resistance of the flux measurement rod compared with the heat spreader used for sample measurement.

If flux is increased, the flux instrument is calibrated to 1%, the temperature measurement is done to ± 0.1 K, and the dimensions are characterized to 0.01 mm the relative measurement uncertainty of plate-to-plate heat transfer is reduced from the current 1.2 to below 0.2.

5.3. Variance

All values presented and used throughout the study were taken as averages of 60 measurements along a single experiment. Although these values varied due to changing environmental conditions throughout the test and the varying power of the laser heat source, their variance was not as significant compared to measurement errors. To limit variance, in the environmental conditions, measurements were taken at night, when the building climate system was not operating. Plexiglas walls were also erected around the sample to stagnate the air immediately surrounding the sample and temperature measurement devices. To achieve steady state heat flux, long measurements were taken and the 60 consecutive values of the most stable data were manually selected.

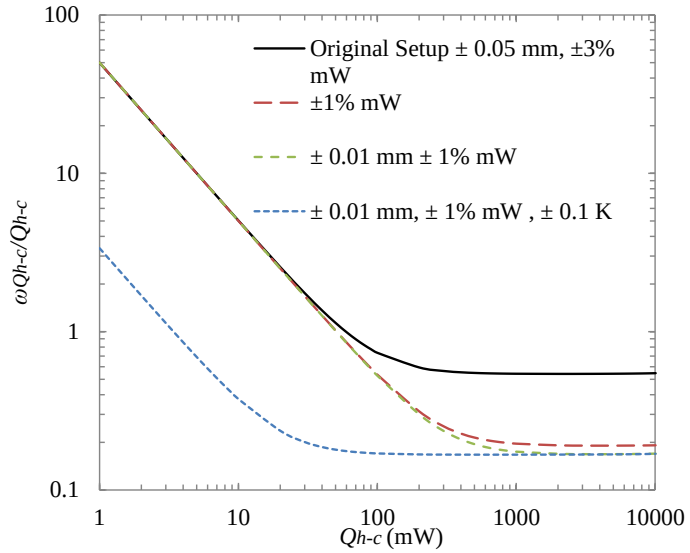

Figure 5.11. Reduction of relative uncertainty by increasing accuracy of Q_i, T, and dimension measurements.

5.4. Summary

In summary, methods were developed to obtain a measurement of heat flux between plane-parallel plates. The relationship between plate separation and radiative heat transfer rate follows the expected trend. On the other hand the experimental uncertainty is on the same order of magnitude as the results, so it difficult to verify or dispute the theoretical relationship between radiative heat transfer and plate separation. Using the same samples and methods the level of uncertainty in these measurements can be reduced by increasing heat flux incident on the sample, calibrating the laser power meter, calibrating thermocouples, and measuring positions of each thermocouple and dimensions of each sample more accurately.

6. CONCLUSIONS AND RECOMMENDATIONS

6.1. Conclusions

For environmental and economic concerns, energy efficiency is of great importance. One approach to increasing energy efficiency is to recover waste heat from high temperature manufacturing processes as electricity using thermophotovoltaic devices which convert heat radiatively emitted as light to an electric potential. Obstacles in radiative energy recovery is the broad spectral emission from which narrow bands can only be converted. The other limit is the blackbody limit of total flux rate. These limit for total radiation exists for transfer between objects separated by distances much greater than the dominant emitted wavelength. For objects in closer proximity than the dominant emitted wavelength according to Plank's blackbody distribution, or the near-field, radiative transfer may exceed the blackbody limit, in narrow wavelength bands due to coupling of surface-phonons. Understanding the near-field could be instrumental in making more efficient and higher capacity thermophotovoltaic devices. The increase in radiation at close proximity has been shown down to the micrometer scale for parallel plates, to tens of nano-meter scale for sphere to plane geometry, and to nanometer distance for tip to plane.

The aim of this thesis was to establish a method for measuring radiative heat transfer between nano-spaced plane-parallel plates. The setup measures two adjacent millimetric sized uniformly nano-spaced plane-parallel silica coated silicon plates. Heat flux is quantified as one plate is heated, and one is cooled at steady state. The temperature measurements are carried out by one temperature probe on each substrate. The heat flux is generated by an external focused laser source. The measurement of flux is made by diverting a percentage of the incoming light to a photodiode. The stabilization of heat flux is achieved by cooling using a passive heat spreader. Measurements were evaluated based on their comparison with theoretically calculated results, which indicate an exponential increase in net radiation heat transfer as plate spacing decreases.

Heat transfer across nano-structured, bonded samples was measured for a plate separation of 100 nm and a plate separation of 200nm. The measurements were in

agreement with the theory. The uncertainties in the heat transfer measurements however were on the order of magnitude of the measured total heat transfer between plates.

6.2. Recommendations and Future Work

For this setup to better quantify the total heat transfer between plates thereby quantifying the different forms of transfer, the quantity of heat flux must be increased to 500 mW incident. A significant difference can be made if the type K thermocouples are replaced by type T thermocouples or by thermistors and calibrating these instruments. The accuracy of the photo-diode and power meter used for incident flux measurement systems can also be calibrated to higher accuracy. The sample dimensions are to be accurately measured so that these dimensions can be used in the measurement analysis. A scanning electron microscope should been used to quantify the sample dimensions.

Thermocouple positioning is very critical in calculations since the surface temperature is calculated based on the position of the thermocouple. Two options for increasing positioning accuracy are, either developing a thermocouple positioning fixture for more consistency, or the position of thermocouples in every experiment should be measured if positioning cannot be consistent. To ensure a central attachment, a marking at the center of the plate edges could be used for visually confirming each thermocouple position. For the second option of measuring the position of thermocouples in every experiment, this can be implemented by taking a photograph using the microscope of the thermocouples' positions on the plates. Using a high precision laser and the 70/30 beam splitter, or an optical instrument which diverts a precisely known portion of light, the power meter can be calibrated to give a higher accuracy measurement than that specified by the manufacturer.

Samples that are not sealed and with known wall or pillar surface area should be prepared and measured to better understand the contribution, or if there is a contribution of conduction through air. Currently the ability of the walls to hold a vacuum between plates is not known. Measuring the conduction of air between nano-spaced plane-parallel plates is also a novel work as it analyzes the effect of conduction over distances approaching the mean free path of air (~40nm).

Using a higher power heat source is a must for reducing the inaccuracy of the measurements. This would greatly reduce the uncertainty in the absorptivity measurement which affects all other measurements. It would allow an extension of the range of this experiment as well. Ideally a 1 W laser with +/- 1% change would be used. This then could be used to calibrate the power meter increasing the accuracy of the flux measurement itself.

Near-field heat transfer measurements are important for showing two effects as predicted by theory, the increase in magnitude of heat transfer and the reduction in spectral width at certain resonances, so the frequency dependence of surface phonon-polariton coupling needs to be measured. One method measure this would be exciting phonons or driving the lattice waves at different frequencies on one of the two plates while monitoring its effect on the adjacent plate. This surface wave in a dielectric material may be excited by applying an alternating electric field across the plate at multiple frequencies. One way to excite the different resonances would be to use a variable high power light source such as a CO_2 laser which has a frequency range above and below the calculated resonance for SiO_2, so it could be used to show not only the magnitude but also the surface phonon-polariton frequency at which there is a much higher rate of radiative heat transfer.

APPENDIX A: EXPERIMENTAL UNCERTAINTY CALCULATIONS

To find the uncertainty interval of *R*, the second-power-equation is used which predicts the result's uncertainty value within ± 10% of the correct value. (Kline and McClintock, 1953) The second-power-equation for any result r with uncertainty interval ω_r which is dependent on $v_1, v_2, \ldots, v_n$ with respective uncertainty intervals $\omega_1, \omega_2, \ldots, \omega_n$ is:

$$\omega_r = \left[\left(\frac{\partial r}{\partial v_1} \omega_1 \right)^2 + \left(\frac{\partial r}{\partial v_2} \omega_2 \right)^2 + \cdots + \left(\frac{\partial r}{\partial v_n} \omega_n \right)^2 \right]^{\frac{1}{2}}. \tag{A.1}$$

Equation (A.1) is applied to all calculated values in all experiments. Applying the second-power-equation to find ω_R, the uncertainty interval of *R*, the equation is as follows.

$$\omega_R = \left[\left(\frac{\omega_{Qmeas}}{Q_{meas}} \right)^2 + \left(\frac{Q_{meas}}{Q_i^2} \omega_{Qi} \right)^2 \right]^{\frac{1}{2}} \tag{A.2}$$

where ω_{Qmeas} and ω_{Qi} are the uncertainty intervals of Q_{meas} and Q_i respectively and are calculated by multiplying the individual measurements by the uncertainty interval of the equipment used to make the measurement as aforementioned. For this experiment ω_R is calculated to be 0.44. When *R* is used in measurements to find Q_i from Q_{meas}, for each experiment, ω_{Qi}, the uncertainty interval of Q_i is calculated:

$$\omega_{Qi} = \left[\left(R\omega_{Qmeas} \right)^2 + \left(Q_{meas}\omega_R \right)^2 \right]^{\frac{1}{2}} \tag{A.3}$$

Following the definitions in Section 4.2, the uncertainty of the measured sample absorptivity is calculated in Equation A.4.

$$\omega_{\alpha} = \left[\left(\frac{\omega_{Qout,cond}}{Q_i} \right)^2 + \left(\frac{\omega_{Qconv}}{Q_i} \right)^2 + \left(\frac{\omega_{Qrad}}{Q_i} \right)^2 + \left(\frac{\alpha\omega_{Qi}}{Q_i} \right)^2 \right]^{\frac{1}{2}} \tag{A.4}$$

By applying the second power equation to Equation 4.3 for $Q_{out,cond}$, $\omega_{Qout,cond}$ is found to be

$$\omega_{Qout,cond} = \left[\begin{array}{l} \left(\frac{Q_{out,cond}}{k_{C11000}} \omega_{kc11000} \right)^2 + \left(\frac{Q_{out,cond}}{A_{Rod}} \omega_{ARod} \right)^2 + \\ + \left(\frac{Q_{out,cond}}{\Delta T_{Rod}} \omega_{\Delta TRod} \right)^2 + \left(\frac{Q_{out,cond}}{\Delta x} \omega_{\Delta x} \right)^2 \end{array} \right]^{\frac{1}{2}} \tag{A.5}$$

The second term in Equation A.4 is defined as

$$\omega_{Qconv} = \left[\left(\omega_{Qh,conv} \right)^2 + \left(\omega_{Qc,conv} \right)^2 \right]^{\frac{1}{2}} \tag{A.6}$$

where,

$$\omega_{Qh,conv} = \left[\left(\Delta T_h \omega_{hhAh} \right)^2 + \left(h_h A_h \omega_{\Delta Th} \right)^2 \right]^{\frac{1}{2}} \tag{A.7}$$

and

$$\omega_{Qc,conv} = \left[\left(\Delta T_C \omega_{hcAc} \right)^2 + \left(h_c A_c \omega_{\Delta Tc} \right)^2 \right]^{\frac{1}{2}} \tag{A.8}$$

The uncertainties of h_hA_h and h_cA_c are as calculated in Equations A.9 and A.10 as;

$$\omega_{hhAh} = \left[\begin{array}{l} \left(\left(lh_v + th_{h,u} + th_{h,d} \right) \omega_w \right)^2 + \left(\left(2lh_v + wh_{h,u} + wh_{h,d} \right) \omega_t \right)^2 + \\ + \left(\left(\left(w + 2t \right) h_v \right) \omega_l \right)^2 + \left(\left(w + 2t \right) l \omega_{hv} \right)^2 + \left(wt\omega_{hh,u} \right)^2 + \left(wt\omega_{hh,d} \right)^2 \end{array} \right]^{\frac{1}{2}} \tag{A.9}$$

$$\omega_{hcAc} = \left[\begin{array}{l} \left(\left(th_{h,u} + th_{h,d}\right)\omega_w\right)^2 + \left(\left(2lh_v + wh_{h,u} + wh_{h,d}\right)\omega_t\right)^2 + \\ + \left(2th_v\omega_l\right)^2 + \left(2tl\,\omega_{hv}\right)^2 + \left(wt\omega_{hh,u}\right)^2 + \left(wt\omega_{hh,d}\right)^2 \end{array} \right]^{\frac{1}{2}} \quad \text{(A.10)}$$

The uncertainties in h_v, $h_{h,u}$, $h_{h,d}$, the respective free convective vertical, horizontal up-facing, and horizontal down-facing heat transfer coefficients for air are;

$$\omega_{hv} = \left[\left(\left(\frac{1.37}{4\left(\Delta T_c\right)^{0.75} l^{0.25}} \right) \omega_{\Delta T} \right)^2 + \left(-\frac{1.37\left(\Delta T_c\right)^{0.25}}{4l^{1.25}}\,\omega_l \right)^2 \right]^{\frac{1}{2}} \quad \text{(A.11)}$$

$$\omega_{hh,u} = \frac{2.49\omega_{\Delta Tc}}{4\Delta T_c^{0.75}} \quad \text{(A.12)}$$

$$\omega_{hh,d} = \frac{1.31\omega_{\Delta Tc}}{4\Delta T_c^{0.75}} \quad \text{(A.13)}$$

The uncertainty of the radiative heat transfer from both plates ω_{Qrad}, and that from each plate individually $\omega_{Qc,rad}$ and $\omega_{Qh,rad}$ are defined in Equations A.14 through A.16.

$$\omega_{Qrad} = \left[\omega_{Qc,rad}^2 + \omega_{h,rad}^2\right]^{\frac{1}{2}} \quad \text{(A.14)}$$

$$\omega_{Qh,rad} = \alpha_{Si}\sigma\left\{\left[\left(T_h^4 - T_{wall}^4\right)\omega_{Ah}\right]^2 + \left(4A_hT_h^3\omega_{Th}\right)^2 + \left(4A_hT_{wall}^3\omega_{Twall}\right)^2\right\}^{\frac{1}{2}} \quad \text{(A.15)}$$

$$\omega_{Qc,rad} = \alpha_{Si}\sigma\left\{\left[\left(T_c^4 - T_{wall}^4\right)\omega_{Ac}\right]^2 + \left(4A_cT_c^3\omega_{Tc}\right)^2 + \left(4A_cT_{wall}^3\omega_{Twall}\right)^2\right\}^{\frac{1}{2}} \quad \text{(A.16)}$$

The uncertainty of $Q_{h\text{-}c}$ is:

$$\omega_{Qh-c} = \left[\omega_{Qout,cond}^2 + \omega_{c,conv}^2 + \omega_{c,rad}^2\right]^{\frac{1}{2}} \quad \text{(A.17)}$$

The uncertainty in total thermal contact resistance, ω_{Jth} is:

$$\omega_{Jth} = \left[\left(\left(\frac{T_h - T_c}{Q_{h-c,cond}} \right) \omega_A \right)^2 + \left(\left(-A \frac{T_h - T_c}{Q_{h-c,cond}^2} \right) \omega_{Qh-c,cond} \right)^2 + \left(-\frac{\omega_{tSi}}{k_{Si}} \right)^2 + \left(-\frac{\omega_{tSiO2}}{k_{SiO2}} \right)^2 \right]^{\frac{1}{2}} \tag{A.18}$$

The uncertainty in area, ω_A, is calculated as;

$$\omega_A = \left[(w\omega_l)^2 + (l\omega_w)^2 \right]^{\frac{1}{2}} \tag{A.19}$$

The uncertainty of the width and length derive from the accuracy of the calipers ± 0.05 mm used to measure these dimensions. For the wafer sandwiches from which 100 nm gap and 200 nm gap samples were diced, the thermal resistances were calculated to be 0.0031 ∓ 0.0014 and 0.0030 ∓ 0.0011 K/mW respectively. Thicknesses t_{Si} and t_{SiO2} are 500 ± 100 μm and 450 ± 10 nm respectively. The thermal resistance value is dependent on the area through which the heat is transferred. The contact areas vary from sample to sample. This is why J_{th}, the area dependent thermal contact resistance, is used as defined in Equation (4.13). This is especially important for the silica-silica interface which in the gapped sample has a contact area (wall to plate) two orders of magnitude below the area of the silica-silica interface in the pure conduction sample.

The uncertainty in the measured surface temperatures are calculated in Equation 4.36 through 4.37.

$$\omega_{Th,surf} = \left[\omega_{Th}^2 + \left(\frac{Q_{h-c}}{A} \right)^2 \left(\left(J_{th}^{'} + \frac{t_{Si}}{k_{Si}} + \frac{t_{SiO2,h}}{k_{SiO2}} \right)^2 \left(\left(\frac{\omega_{Qh-c}}{Q_{h-c}} \right)^2 + \left(\frac{\omega_A}{A} \right)^2 \right) + \omega_{Jth}{}^2 + \left(\frac{\omega_{tSi}}{k_{Si}} \right)^2 + \left(\frac{\omega_{tSiO2}}{k_{SiO2}} \right)^2 \right) \right]^{\frac{1}{2}} \tag{A.20}$$

$$\omega_{Tc,surf} = \left[\omega_{Tc}^2 + \left(\frac{Q_{h-c}}{A} \right)^2 \left(\begin{array}{l} \left(J_{th}^{'} + \frac{t_{Si}}{k_{Si}} + \frac{t_{SiO2,c}}{k_{SiO2}} \right)^2 \left(\left(\frac{\omega_{Qh-c}}{Q_{h-c}} \right)^2 + \left(\frac{\omega_A}{A} \right)^2 \right) + \\ + \omega_{Jth}{}^2 + \left(\frac{\omega_{tSi}}{k_{Si}} \right)^2 + \left(\frac{\omega_{tSiO2}}{k_{SiO2}} \right)^2 \end{array} \right) \right]^{\frac{1}{2}} \quad \text{(A.21)}$$

The uncertainty of $Q_{h\text{-}c,rad}$ as defined in Equation 4.17 is;

$$\omega_{Qh-c,rad} = \left(\omega_{Q_{h-c}}^2 + \omega_{Qh-c,air}^2 + \omega_{Qh-c,wall}^2 \right)^{\frac{1}{2}} \quad \text{(A.22)}$$

REFERENCES

Agilent Technologies, 2009, *Agilent 34970A/34972A Data Aquisition / Switch Unit*, Santa Clara.

Arpacı, V.S., A. Selamet, and S.-H. Kao, 2000, *Introduction to Heat Transfer*. Prentice Hall, Upper Saddle River.

ASTM International, 2012, "E230/E230M Standard Specification and Temperature-Electromotive Force (EMF) Tables for Standardized Thermocouples", West Conshohocken.

Basu, S., Y.B. Chen, and Z.M. Zhang, 2006, "Microscale Radiation in Thermophotovoltaic Devices - a Review", *International Journal of Energy Resources*, Vol. 31, pp. 681-716.

Basu, S., and Z.M. Zhang, 2009, "Maximum Energy Transfer in Near-Field Thermal Radiation at nanometer distances", *Journal of Applied Physics* Vol. 105, pp. 1-6.

Beer, F.B., E.R. Johnston, J.T. DeWolf, and D.F. Mazurek, 2011, *Mechanics of Materials*, McGraw-Hill, New York.

Callister, W.D., 2007, *Materials Science and Engineering an Introduction*, John Wiley & Sons, New York.

Coutts, T.J., and M.C. Fitzgerald, 1998, "Thermophotovoltaics", *Scientific American*, Vol. 279, No. 3, pp. 68-69.

Dalola, S., M. Ferrari, V. Ferrari, M. Guizzetti, D. Marioli, and A. Taroni, 2010, "Characterization of Thermoelectric Modules for Powering Autonomous Sensors", *IEEE Transactions on Instrumentation and Measurement*, Vol. 58, No.1, pp. 99-107.

Davies, R., S.A. Mathias, J. Moss, S. Hustoft, and L. Newport, 2012, "Hydrolic Fractures, How Far Can They Go?", *Marine and Petroleum Geology.* Vol. 37, No. 1, pp. 1-6.

DiMatteo, R., P. Greiff, S.L. Finberg, K.A. Young-Waithe, H.K. Choy, M.M. Masaki, and C.G. Fonstad, 2001, "Enhanced Photogeneration of Carriers in a Semiconductor via Coupling", *Applied Physics Letters*, Vol. 79, No. 12, pp. 1894-1896.

Domoto, G.M., R.F. Boehm, and C.L. Tien, 1970, "Experimental Investigation of Radiative Transfer Between Metallic Surfaces at Cryogenic Temperatures", In: ASME Heat Transfer Division, *American Society of Mechanical Engineers Winter Annual Meeting*, Los Angeles, CA, 1969 Transactions of the ASME, New York.

Edmund Optics Inc., 2011, *Circular Variable Filters*, http://www.edmundoptics.com, accessed at October 2011.

Francoeur, M., M.P. Mengüç, and R. Vaillon, 2008, "Near-field Radiative Heat Transfer Enhancement via Surface Phonon Polaritons Coupling in Thin Films", *Applied Physics Letters*, Vol. 9, No. 043109, pp. 1-3.

Green, M.A., and M. Keevers, 1995, "Optical Properties of Intrinsic Silicon at 300K", *Progress in Photovoltaics*, Vol. 3, No. 3, pp. 189-192.

Han, L.H., X.G. Liang, and Y. Huang, 2005, "Thermal Radiation Characteristics of Plane Parallel SiC Wafer", *Chinese Science Bulletin*, Vol. 50, No. 4, pp. 295-298.

Hargreaves, C.M., 1969, "Anomalous Radiative Transfer Between Closely Spaced Bodies", *Physics Letters*, Vol. 30A, No. 9, pp. 491-492.

Hopcroft, M.A., W.D. Nix, and T.W. Kenny, 2010, "What is the Young's Modulus of Silicon?", *Journal of Microelectromechanical Systems*, Vol. 19, No. 2, pp. 229-238.

Hu, L., A. Narayanaswamy, X. Chen, and G. Chen, 2008, “Near-Field Thermal Radiation Between Closely Spaced Glass Plates Exceeding Planck's Blackbody Radiation Law”, *Applied Physics Letters*, Vol. 92, No. 133106, pp. 1-3.

Kasap, S.O., 2001, *Optoelectronics and Photonics: Principles and Practice*, Prentice Hall Inc., Upper Saddle River.

Kittel, A., W. Müller-Hirsch, J. Parisi, S.A. Biehs, D. Reddig, and M. Holthaus, 2005, “Near Field Heat Transfer in Scanning Thermal Microscope”, *Physical Review Letters*, Vol. 95, No. 224301 pp. 1-4.

Kline, S.J., and F.A. McClintock, 1953, “Describing Uncertainties in Single-Sample Experiments”, *Mechanical Engineering*, Vol. 75, pp. 3-8.

Kothandaraman, C.P., and S. Subramanyan, 1975, *Heat and Mass Transfer Data Book*, John Wiley & Sons, New York.

Lemmon, E.W., and R.T. Jacobsen, 2004, “Viscosity and Thermal Conductivity Equations for Nitrogen Oxygen Argon and Air”, *International Journal of Thermophysics*, Vol. 25, pp. 21-69.

Martin, Y., C.C. Williams, and H.K. Wickramasinghe, 1988, “Techniques for Microcharacterization of Materials”, *Scanning Microscopy*, Vol. 2, No. 1, pp. 3-8.

Martineau, K., 2012, *Ohio Quakes Probably Triggered by Waste Disposal Well, Say Seizmologists*, http://www.ldeo.columbia.edu/news-events/seismologists-link-ohio-earthquakes-waste-disposal-wells, accessed at July 2012.

MolTech GmbH World of Crystals, 2005, *Crystal quarts (SiO2) and fused silica*, http://www.mt-berlin.com/frames_cryst/descriptions/ quartz%20.htm, accessed at December 2011.

Narayanaswamy, A., S. Shen, and G. Chen, 2008, "Near-Field Radiative Heat Transfer Between a Sphere and a Substrate", *Physical Review B*, Vol. 78, No. 115303, pp. 1-4.

Narayanaswamy, A., and G. Chen, 2004, "Thermal Emission Control With One-Dimensional Metallodielectric Photonic Crystals", *Physical Review B*, Vol. 70, No. 125101, pp. 1-4.

National Instruments, 2010, *Thermocouple Accuracy Table by Type and Temperature*, http://digital.ni.com, accessed at December 2011.

Nextreme Thermal Solutions, 2009, *UPF4 Optocooler Preliminary Data Sheet*, www.nextreme.com, accessed at December 2010.

Nozik, A.J., 2002, "Quantum dot Solar Cells", *Phisica E*, Vol. 14, pp. 115-120.

Ottens, R.S., V. Quetschke, S. Wise, A.A. Alemi, R. Lundock, G. Mueller, D.H.Reitze, D.B. Tanner, and B.F. Whiting, 2011, "Near Field Radiative Heat Transfer Between Macroscopic Planar Surfaces", *Phys. Rev. Lett.*, Vol. 107, No.1, pp. 1-4.

Palik, E.D., 1998, *Handbook of Optical Constants*, Academic Press, San Diego.

Rousseau, E., A. Siria, G. Jourdan, S. Volz, F. Comin, J. Chevrier, and J.J. Greffet, 2009, "Radiative Heat Transfer at the Nanoscale", *Nature Photonics*,Vol. 3, No. 9, pp. 514-517.

Serway, R.A., and J.W. Jewett, 2008, *Physics*, Brooks/Cole, Australia.

Shen, S., A. Narayanaswamy, and G. Chen, 2009, "Surface Phonon Polaritons Mediated Energy Transfer Between Nanoscale Gaps", *Nano Letters*, Vol. 9, No. 8, pp. 2909-2913.

Howell, J.R., R. Siegel, and M.P. Mengüç, 2011, *Thermal Radiation Heat Transfer*, CRC Press, Boca Raton.

Skoplaki, E., and J.A. Palyvos, 2008, "On the Temperature Dependence of Photovoltaic Module Electrical Performance: A Review of Efficiency/Power Correlations", *Solar Energy*, Vol. 83, No. 5, pp. 614-624.

Thorlabs, 2012, *C-Series Photodiode Power Sensors*, http://www.thorlabs.de/New Group Page9.cfm ?ObjectGroup_Id=3328&popupcart=yes, accessed at January 2012.

Timoshenko, S., and S. Woinowsky-Krieger, 1959, *Theory of plates and shells.* McGraw-Hill Inc., New York.

Williams, C.C., and H.K. Wickramasinghe, 1986, "Scanning thermal profiler", *Applied Physics Letters*, Vol. 49, No. 23, pp. 1587-1589.

Xu, J.B., K. Läuger, R. Möller, K. Dransfeld, and I.H. Wilson, 1994, "Heat transfer Between Two Metallic Surfaces at Small Distances", *Journal of Applied Physics*, Vol. 76, No. 11, pp. 7209-7216.

Zoback, M., S. Kitasei, and B. Copithorne, 2010, *Addressing the Environmental Risks from Shale Gas Development*, http://efdsystems.org/Portals/25/Hydraulic%20Fracturing %20Paper%20-%20World%20Watch.pdf, accessed at July 2012.